Materials & Design 233 (2023) 112228

Contents lists available at ScienceDirect

Materials & Design

journal homepage: www.elsevier.com/locate/matdes

Hydration kinetics of Portland cement shifting from silicate to aluminate dominance based on multi-mineral reactions and interactions

Yang Liu [a,b], Muyu Liu [a,c,*], Hua Li [d,*], Guitao Luo [a,b], Hongbo Tan [c], Qimin Liu [a,b]

[a] School of Civil Engineering and Architecture, Wuhan University of Technology, Wuhan 430070, China
[b] Hubei Key Laboratory of Roadway Bridge & Structure Engineering, Wuhan University of Technology, Wuhan 430070, China
[c] State Key Laboratory of Silicate Materials for Architectures, Wuhan University of Technology, Wuhan 430070, China
[d] School of Mechanical and Aerospace Engineering, Nanyang Technological University, Singapore 639798, Singapore

ARTICLE INFO

Keywords:
Portland cement
Kinetics shift
Interaction
Mineral composition

ABSTRACT

A theoretical model for cement hydration was proposed to study multi-mineral reactive transport processes under various mineral compositions and determine the effect of multi-mineral reactions and interactions on cement hydration kinetics shifting from silicate to aluminate dominance. The reaction rates of each mineral dissolution, product precipitation, ionic diffusion, and adsorption were calculated individually through the degrees of undersaturation and supersaturation associated with the ionic concentration, all of which were coupled in the modified Poisson–Nernst–Planck equation. The hydration heat flow was then theoretically calculated by the superposition of the reaction rates of silicate and aluminate phases, which was derived from the calculated ionic concentration. The model was validated by comparison with experimental data obtained under various conditions, showing consistency. The combined effect of multi-mineral reactions and interactions on hydration kinetics was investigated using the model, and the results indicated that (1) faster dissolution of gypsum or a higher ratio of tricalcium aluminate to tricalcium silicate leads to a larger time interval between silicate and aluminate peaks; (2) faster precipitation of calcium silicate hydrate results in a more significant difference between silicate and aluminate peaks; and (3) the sulfate ion retards cement hydration kinetics shifting from silicate to aluminate dominance.

1. Introduction

To satisfy these requirements, various types of Portland cement (PC) with different mineral compositions are widely used in construction engineering [1,2]. The main mineral compositions of PC are tricalcium silicate (C_3S), tricalcium aluminate (C_3A), tetracalcium aluminoferrite (C_4AF), and tricalcium silicate (C_2S). In general, PC hydration is a complex process involving the dissolution, diffusion, precipitation, and adsorption of each mineral phase, hydration product, and ionic species [2,3]. Although numerous investigations have revealed the hydration mechanisms of pure C_3S, C_3A, C_4AF, C_2S, and gypsum, as well as the interactions among the mineral phases [4–13], studies on the hydration kinetics of PC are still insufficient regarding the various mineral phases within the clinker. In particular, the combined effect of multi-mineral dissolution, diffusion, precipitation, adsorption, and interactions on the hydration kinetics shifting from silicate to aluminate is difficult to study solely using experiment-based approaches because of the time- and spatially dependent behavior of the reaction kinetics of PC paste. Because of the difference in the reaction kinetics of each clinker mineral and hydration product (calcium silicate hydrate (C-S-H), portlandite (CH), ettringite (AFt), and monosulfoaluminate (AFm)), the reaction rate of each phase in the PC paste must be calculated individually with their local thermodynamic state instead of using a simplified average or proportional rate for all phases. In addition, the dissolution, diffusion, precipitation, and adsorption behaviors must be combined and coupled via ionic species in the theoretical computations used for hydration simulations. Thus, the reactive transport model can be used to study the combined effect of multi-mineral dissolution, diffusion, precipitation, adsorption, and interactions on the hydration kinetics of shifting from silicate to aluminate dominant cement with different mineral compositions.

Recently, Bentz simulated cement hydration with different mineral compositions using cellular automata and random walk methods; however, the chemical kinetics and thermodynamics were not

* Corresponding authors at: School of Civil Engineering and Architecture, Wuhan University of Technology, Wuhan 430070, China (M. Liu).
E-mail addresses: liumuyu@whut.edu.cn (M. Liu), lihua@ntu.edu.sg (H. Li).

https://doi.org/10.1016/j.matdes.2023.112228
Received 6 April 2023; Received in revised form 10 July 2023; Accepted 6 August 2023
Available online 18 August 2023

considered [14]. Breugel *et al.* proposed a computer-based numerical model to simulate the chemical reaction and microstructure formation in hydrated Portland cement [15]. Bishnoi and Scrivener developed a new modeling platform to simulate cement hydration and microstructure development, in which grid subdivisions were used to calculate the interaction of all particles [16]. Bullard *et al.* proposed a reaction-transport model to simulate chemical reactions and ionic diffusion during cement hydration; however, the interaction between C_3S and the C_3A hydration reaction was not considered [17]. Le *et al.* proposed a multi-component model to simulate the growth and microstructural evolution of cement hydration products without considering the effect of the pore solution on the dissolution and precipitation rates [18]. Ma *et al.* developed a kinetics model combining the modified Avrami equation with Bentz's model to predict the hydration degree of a mineral composition that lacks the reaction kinetics of dissolution and adsorption [19]. Holmes *et al.* proposed a thermodynamic model that combined PHREEQC with HYDCEM to predict the evolution of the phase assemblage and pore solution without interactions between the mineral phases in the clinker [20].

However, current studies on this topic have two main issues: (1) the reaction rate of each mineral dissolution, product precipitation, ionic diffusion, and ionic adsorption was not calculated individually via ionic concentration, which is unable to provide an accurate calculation of the combined effect of multi-mineral reactions and interactions during cement hydration; and (2) the hydration heat flow was not calculated based on the reaction rate of the silicate and aluminate phases, which is unable to quantitatively predict the hydration kinetics shifting from silicate to aluminate dominance.

Therefore, a theoretical model for cement hydration was developed to simulate the multi-mineral dissolution-diffusion-precipitation-adsorption reactions and interactions during PC hydration. In the model, the reaction rates of mineral dissolution, product precipitation, ionic diffusion, and adsorption were calculated and coupled using the ionic concentration. Based on the calculated ionic concentration, the reaction rates of the silicate and aluminate phases were used to establish a theoretical formula for the hydration heat flow, which was also compared with published experimental data for various mineral compositions, specific surface areas (SSAs), water-to-cement ratios (w/c), and curing temperatures. Subsequently, the effects of multi-mineral dissolution, diffusion, precipitation, and adsorption behaviors on hydration kinetics were studied individually and in combination. Finally, the peak values and times of the silicate and aluminate phase reactions

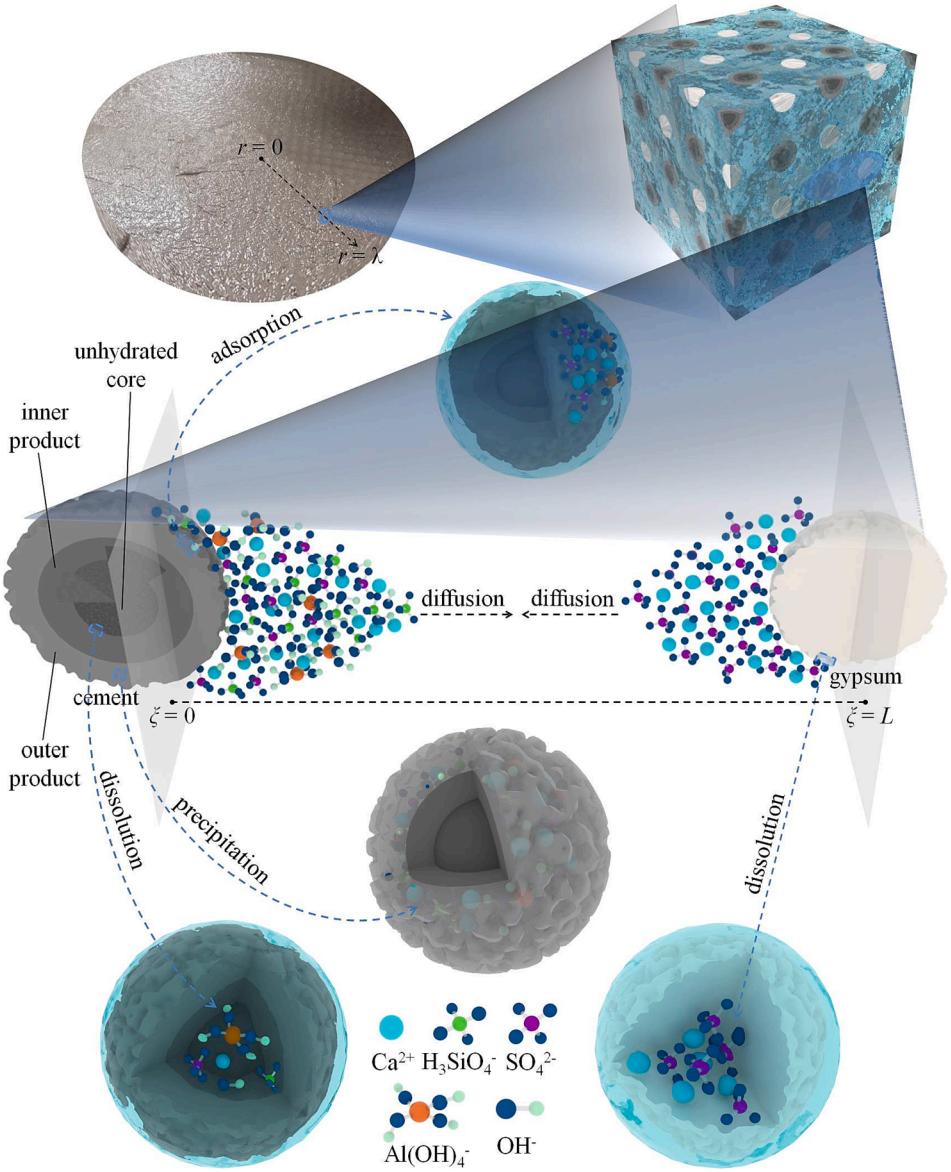

Fig. 1. Schematic diagram of chemical reactions during Portland cement hydration.

were quantitatively analyzed to investigate the combined effect of these behaviors on the hydration kinetics of shifting from silicate to aluminate dominance for cement with different gypsum, C_3A, and C_3S contents.

2. Multi-mineral reactions and interactions for Portland cement hydration

To gain a clear insight into the multi-mineral reactions and interactions, the reaction rates of mineral dissolution, product precipitation, ionic diffusion, and adsorption were calculated and coupled in the governing equation for the hydration reaction between the cement and gypsum grains, as shown in Fig. 1. The cement particles are assumed to be uniform in size and distributed within the paste [21]. Moreover, the electric potential distribution between the grains and the temperature distribution in the paste were characterized using the corresponding equation. The hydration heat flow was calculated using the superposition of the silicate and aluminate phase reactions to investigate the kinetic shift from silicate- to aluminate-dominant cement hydration. The chemical reactions for cement hydration are given as follows [22–26]:

$$3CaO{\cdot}SiO_2 + 4H_2O \rightarrow 3Ca^{2+} + H_3SiO_4^- + 5OH^- \quad (1)$$

$$3CaO{\cdot}Al_2O_3 + 6H_2O \rightarrow 3Ca^{2+} + 2Al(OH)_4^- + 4OH^- \quad (2)$$

$$4CaO{\cdot}Al_2O_3{\cdot}Fe_2O_3 + 10H_2O \rightarrow 4Ca^{2+} + 2Al(OH)_4^- + 6OH^- + 2Fe(OH)_3 \quad (3)$$

$$2CaO{\cdot}SiO_2 + 3H_2O \rightarrow 2Ca^{2+} + H_3SiO_4^- + 3OH^- \quad (4)$$

$$CaSO_4{\cdot}2H_2O \rightarrow Ca^{2+} + SO_4^{2-} + 2H_2O \quad (5)$$

$$5Ca^{2+} + 3H_3SiO_4^- + 7OH^- \rightarrow (CaO)_5{\cdot}(SiO_2)_3{\cdot}(H_2O)_8 \quad (6)$$

$$Ca^{2+} + 2OH^- \rightarrow Ca(OH)_2 \quad (7)$$

$$6Ca^{2+} + 2\left[Al, Fe(OH)_4^-\right] + 3SO_4^{2-} + 4OH^- + 26H_2O \rightarrow 3CaO{\cdot}[Al_2O_3, Fe_2O_3]{\cdot}3CaSO_4{\cdot}32H_2O \quad (8)$$

$$C_6(A,F)\overline{S}_3H_{32} + 6Ca^{2+} + 4\left[Al, Fe(OH)_4^-\right] + 8OH^- \rightarrow 3C_4(A,F)\overline{S}H_{12} + 8H_2O \quad (9)$$

where $3CaO{\cdot}[Al_2O_3, Fe_2O_3]{\cdot}3CaSO_4{\cdot}32H_2O$ ($C_6(A,F)\overline{S}_3H_{32}$) and $C_4(A,F)\overline{S}H_{12}$ represent ettringite (AFt) and monosulfate (AFm), respectively.

2.1. Reaction kinetics for each phase and interactions

(a) Ionic diffusion coupled with dissolution, precipitation, and adsorption between grains.

In this subsection, a reaction rate formula was developed for mineral dissolution, product precipitation, ionic diffusion, and adsorption. The interactions between the dissolution and precipitation of the different mineral phases were also considered in the reaction rate equations. Moreover, the dissolution, diffusion, precipitation, and adsorption behaviors were coupled via the ionic concentration in the Poisson–Nernst–Planck (PNP) equation [27] as follows:

$$\dot{c}_k + \nabla{\cdot}\mathbf{J}_k = v_{cem}^k + n_k^{gyp}v_{gyp} + n_k^{CSH}v_{CSH} + n_k^{CH}v_{CH} + n_k^{AFt}v_{AFt} + n_k^{AFm}v_{AFm} + v_{ads}^k \quad (10)$$

$$\mathbf{J}_k = -D_k\left[\nabla c_k + \frac{z_kF}{RT}c_k\nabla\psi + c_k\nabla\ln\gamma_k\right] \quad k = Ca^{2+}, H_3SiO_4^-, Al(OH)_4^-, OH^-, SO_4^{2-} \quad (11)$$

where c_k, $\mathbf{J}_k$, D_k, z_k, and γ_k denote the ionic concentration (mM), diffusion flux (mol m^{-2} s^{-1}), diffusion coefficient (m^2 s^{-1}), valence number, and chemical activity coefficient of the kth ionic species, respectively. $\nabla(\cdot)$ and $\nabla(\cdot)$ represent the divergence and gradient with respect to ξ, respectively. v_{cem}^k is the generation rate of the kth ionic species owing to cement dissolution (mol m^{-3} s^{-1}), as described in Eqs. (1)–(4). n_k^{gyp}, n_k^{CSH}, n_k^{CH}, n_k^{AFt}, and n_k^{AFm} are the molar stoichiometric coefficients of the kth ionic species obtained from the dissolution of gypsum and C-S-H, CH, AFt, and AFm precipitation as described in Eqs. (5)–(9), respectively. v_{gyp}, v_{CSH}, v_{CH}, v_{AFt}, and v_{AFm} are the dissolution rate of gypsum and the precipitation rate of C-S-H, CH, AFt, and AFm (mol m^{-3} s^{-1}), respectively. v_{ads}^k is the ionic species adsorption rate (mol m^{-3} s^{-1}). T, ψ, F, and R are the absolute temperature (K), electric potential (V), Faraday's constant (C mol^{-1}), and universal gas constant (J mol^{-1} K^{-1}), respectively. The chemical activity (γ_k) can be expressed by the Debye–Hückel model [28].

The first term (v_{cem}^k) on the right side of Eq. (10) represents the source term for the generation of ionic species (Ca^{2+}, $H_3SiO_4^-$, $Al(OH)_4^-$, and OH^-) because of the dissolution of cement given by Eqs. (1)–(4). The ionic species generation rate during cement dissolution (v_{cem}^k) can be described using the following equation:

$$v_{cem}^k = (n_k^{C_3S}{\cdot}v_{C_3S} + n_k^{C_3A}{\cdot}v_{C_3A} + n_k^{C_4AF}{\cdot}v_{C_4AF} + n_k^{C_2S}{\cdot}v_{C_2S}) \quad (12)$$

where $n_k^{C_3S}$, $n_k^{C_3A}$, $n_k^{C_4AF}$, and $n_k^{C_2S}$ represent the molar stoichiometric coefficients of the kth ionic species released from the dissolution reactions of C_3S, C_3A, C_4AF, and C_2S, respectively, as described in Eqs. (1)–(4). v_{C_3S}, v_{C_3A}, v_{C_4AF}, and v_{C_2S} denote the dissolution rate of C_3S, C_3A, C_4AF, and C_2S (mol m^{-3} s^{-1}), respectively.

The first term ($n_k^{C_3S}{\cdot}v_{C_3S}$) on the right side of Eq. (12) represents the C_3S dissolution rate, which is used as the source term for the generation of ionic species (Ca^{2+}, $H_3SiO_4^-$, and OH^-), as given by Eq. (1). Recently, interactions between the C_3A and C_3S hydration reactions have been observed in many experimental studies, and several mechanisms have been proposed to explain the retarding effect of aluminum on the C_3S hydration reaction, such as C-A-S-H phase precipitation [29] and the adsorption of Al ions on the surface of C_3S [11]. Thus, the dissolution rate of pure phase C_3S was modified by considering the aluminum inhibition effect based on mineral dissolution investigations [30,31]. The C_3S dissolution rate (v_{C_3S}) is given by [24,32,33]:

$$v_{C_3S} = m_{C_3S}\%{\cdot}O_V^{B-cem}k_{C_3S}\frac{K_f^{C_3S-Al(OH)_4^-}}{K_f^{C_3S-Al(OH)_4^-} + a_{Al(OH)_4^-}}(1-\beta_{C_3S}) \quad (13)$$

$$O_V^{B-cem} = \frac{SSA_{cement}}{\frac{w/c}{\rho_{H_2O}} + \frac{1}{\rho_{cement}} + \frac{m_{gypsum}\%}{\rho_{gypsum}}} \quad (14)$$

$$\beta_{C_3S} = \frac{\{c_{Ca^{2+}}\}^3\left\{c_{H_3SiO_4^-}\right\}\{c_{OH^-}\}^5}{K_{C_3S}} \quad (15)$$

$$\{c_k\} = \frac{c_k\gamma_k}{\rho_{H_2O}c_0} \quad (16)$$

where $m_{C_3S}\%$, k_{C_3S}, K_{C_3S}, $K_f^{C_3S-Al(OH)_4^-}$, $\{c_k\}$, and c_0 represent the C_3S

content percentage, C_3S dissolution rate constant (mol m^{-2} s^{-1}), C_3S solubility constant, complexation stability constant for aluminum on the silicate surface, activity of ionic species, and molal concentration in the standard state (mol kg^{-1}) [34,35], respectively. O_V^{B-cem}, SSA_{cement}, w/c, and m_{gypsum}% denote the surface area of the cement grain per unit volume of paste (m^{-1}) [36], cement specific surface area (m^2 kg^{-1}), water-to-cement ratio, and gypsum content percentage, respectively. ρ_{cement}, ρ_{H_2O}, and ρ_{gypsum} represent the densities of cement, water, and gypsum (kg m^{-3}), respectively.

The second term ($n_k^{C_3A} \cdot v_{C_3A}$) on the right side of Eq. (12) represents the C_3A dissolution rate used as the source term for the generation of the ionic species (Ca^{2+}, $Al(OH)_4^-$, and OH^-), as given by Eq. (2). As indicated in the literature, the retarding effect of the calcium-sulfate ion pair adsorption was considered in the C_3A dissolution rate (v_{C_3A}) and is given by [37,38]

$$v_{C_3A} = m_{C_3A}\% \cdot O_V^{B-cem} k_{C_3A} \frac{K_f^{C_3A-Ca^{2+}-SO_4^{2-}}}{K_f^{C_3A-Ca^{2+}-SO_4^{2-}} + a_{Ca^{2+}} \cdot a_{SO_4^{2-}}} (1 - \beta_{C_3A}) \tag{17}$$

$$\beta_{C_3A} = \frac{\{c_{Ca^{2+}}\}^3 \{c_{Al(OH)_4^-}\}^2 \{c_{OH^-}\}^4}{K_{C_3A}} \tag{18}$$

where m_{C_3A}%, k_{C_3A}, K_{C_3A}, and $K_f^{C_3A-Ca^{2+}-SO_4^{2-}}$ represent the C_3A content percentage, C_3A dissolution rate constant (mol m^{-2} s^{-1}), C_3A solubility constant, and equilibrium constant of the calcium-sulfate ion pair absorbed on the C_3A surface, respectively.

The third term ($n_k^{C_4AF} \cdot v_{C_4AF}$) on the right side of Eq. (12) represents the C_4AF dissolution rate, which is used as the source term for the generation of ionic species (Ca^{2+}, $Al(OH)_4^-$, and OH^-), as given by Eq. (3). The C_4AF dissolution rate (v_{C_4AF}) is given by [38,39]:

$$v_{C_4AF} = m_{C_4AF}\% \cdot O_V^{B-cem} k_{C_4AF} (1 - \beta_{C_4AF}) \tag{19}$$

$$\beta_{C_4AF} = \frac{\{c_{Ca^{2+}}\}^4 \{c_{Al(OH)_4^-}\}^2 \{c_{OH^-}\}^6}{K_{C_4AF}} \tag{20}$$

where m_{C_4AF}%, k_{C_4AF}, and K_{C_4AF} represent the C_4AF content percentage, C_4AF dissolution rate constant (mol m^{-2} s^{-1}), and C_4AF solubility constant, respectively.

The fourth term ($n_k^{C_2S} \cdot v_{C_2S}$) on the right side of Eq. (12) represents the C_2S dissolution rate used as the source term for the generation of the ionic species (Ca^{2+}, $H_3SiO_4^-$, and OH^-), as given by Eq. (4). The C_2S dissolution rate (v_{C_2S}) is given by [7]:

$$v_{C_2S} = m_{C_2S}\% \cdot O_V^{B-cem} k_{C_2S} (1 - \beta_{C_2S}) \tag{21}$$

$$\beta_{C_2S} = \frac{\{c_{Ca^{2+}}\}^2 \{c_{H_3SiO_4^-}\} \{c_{OH^-}\}^3}{K_{C_2S}} \tag{22}$$

where m_{C_2S}%, k_{C_2S}, and K_{C_2S} represent the C_2S content percentage, C_2S dissolution rate constant (mol m^{-2} s^{-1}), and C_2S solubility constant, respectively.

The second term ($n_k^{gyp} v_{gyp}$) on the right side of Eq. (10) represents the gypsum dissolution rate used as the source term for the generation of the ionic species (Ca^{2+} and SO_4^{2-}) given by Eq. (5). The gypsum dissolution rate (v_{gyp}) is given by [40]:

$$v_{gyp} = k_{gypsum} O_V^{B-gypsum} (1 - \beta_{gypsum}) \tag{23}$$

$$\beta_{gypsum} = \frac{\{c_{Ca^{2+}}\}^1 \{c_{SO_4^{2-}}\}^1}{K_{gypsum}} \tag{24}$$

$$O_V^{B-gypsum} = \frac{SSA_{gypsum}}{\frac{w/c}{m_{gypsum}\% \cdot \rho_{H_2O}} + \frac{1}{m_{gypsum}\% \cdot \rho_{cement}} + \frac{1}{\rho_{gypsum}}} \tag{25}$$

where k_{gypsum}, $O_V^{B-gypsum}$, K_{gypsum}, and SSA_{gypsum} denote the gypsum dissolution rate constant (mol m^{-2} s^{-1}), surface area of gypsum grains per unit volume of paste (m^{-1}) [36], gypsum solubility constant, and gypsum specific surface area (m^2 kg^{-1}), respectively.

The third term ($n_k^{CSH} v_{CSH}$) on the right side of Eq. (10) represents the sink term for the ionic species (Ca^{2+}, $H_3SiO_4^-$, and OH^-) owing to the C-S-H precipitation given by Eq. (6). The C-S-H precipitation rate (v_{CSH}) depends on the degree of supersaturation (β_{CSH}), which can be expressed as the ratio of the ion activity product (Q_{CSH}) to the solubility constant (K_{CSH}) as follows [24,32,33,41]:

$$v_{CSH} = \frac{K_f^{CSH-Ca^{2+}-SO_4^{2-}}}{K_f^{CSH-Ca^{2+}-SO_4^{2-}} + a_{Ca^{2+}} \cdot a_{SO_4^{2-}}} k_{CSH} O_V^{B-cem} (\beta_{CSH} - 1) \tag{26}$$

$$\beta_{CSH} = \frac{\{c_{Ca^{2+}}\}^5 \{c_{H_3SiO_4^-}\}^3 \{c_{OH^-}\}^7}{K_{CSH}} \tag{27}$$

where k_{CSH}, K_{CSH}, and $K_f^{CSH-Ca^{2+}-SO_4^{2-}}$ denote the C-S-H precipitation rate constant (mol m^{-2} s^{-1}), C-S-H solubility constant, and equilibrium constant of the calcium-sulfate ion pair absorbed on the C-S-H surface, respectively.

The fourth term ($n_k^{CH} v_{CH}$) on the right side of Eq. (10) represents the sink term used for the ionic species (Ca^{2+} and OH^-) owing to CH precipitation given by Eq. (7), and the CH precipitation rate (v_{CH}) is given by [33]:

$$v_{CH} = k_{CH}(\beta_{CH} - 1) \tag{28}$$

$$\beta_{CH} = \frac{\{c_{Ca^{2+}}\}^1 \{c_{OH^-}\}^2}{K_{CH}} \tag{29}$$

where k_{CH} and K_{CH} denote the CH precipitation rate constant (mol m^{-3} s^{-1}) and the CH solubility constant, respectively.

The fifth term ($n_k^{AFt} v_{AFt}$) on the right side of Eq. (10) represents the sink term used for the ionic species due to ettringite precipitation, which consumes Ca^{2+}, $Al(OH)_4^-$, OH^-, and SO_4^{2-}, as given by Eq. (8). The ettringite precipitation rate (v_{AFt}) is [42,43]

$$v_{AFt} = k_{AFt} O_V^{B-cem} (\beta_{AFt} - 1) \tag{30}$$

$$\beta_{AFt} = \frac{\{c_{Ca^{2+}}\}^6 \{c_{Al(OH)_4^-}\}^2 \{c_{SO_4^{2-}}\}^3 \{c_{OH^-}\}^4}{K_{AFt}} \tag{31}$$

where k_{AFt} and K_{AFt} denote the ettringite precipitation rate constant (mol m^{-2} s^{-1}) and ettringite solubility constant, respectively.

The sixth term ($n_k^{AFm} v_{AFm}$) on the right side of Eq. (10) represents the sink term used for the ionic species due to AFm precipitation, which consumes Ca^{2+}, $Al(OH)_4^-$, and OH^-, as shown in Eq. (9). Thus, the AFm precipitation rate (v_{AFm}) can be given as follows [44,45]:

$$v_{AFm} = k_{AFm}\left(\{c_{Ca^{2+}}\}^2 \{c_{Al(OH)_4^-}\}^{4/3} \{c_{OH^-}\}^{8/3} - K_{AFm}\right) \tag{32}$$

where k_{AFm} and K_{AFm} denote the AFm precipitation rate constant (mol m^{-3} s^{-1}) and AFm solubility constant, respectively.

The seventh term (v_{ads}^k) on the right side of Eq. (10) represents the sink term used for the adsorption of ionic species that consume Ca^{2+}, $Al(OH)_4^-$, and SO_4^{2-} in the solution during the cement hydration reaction. The ionic species adsorption rate (v_{ads}^k) is given by [46]. A detailed formulation of v_{ads}^k is presented in Eqs. (S1)–(S10) (Supporting Information).

$$v_{ads}^{Ca^{2+}} = k_{ads}^{Ca^{2+}} c_{Ca^{2+}} e^{-k_{ads}^{Ca^{2+}} \cdot t} \tag{33}$$

$$v_{ads}^{Al(OH)_4^-} = k_{ads}^{Al(OH)_4^-} c_{Al(OH)_4^-} e^{-k_{ads}^{Al(OH)_4^-} \cdot t} \tag{34}$$

$$v_{ads}^{SO_4^{2-}} = k_{ads}^{SO_4^{2-}} c_{SO_4^{2-}} e^{-k_{ads}^{SO_4^{2-}} \cdot t} \tag{35}$$

where $k_{ads}^{Ca^{2+}}$, $k_{ads}^{Al(OH)_4^-}$, and $k_{ads}^{SO_4^{2-}}$ are the ionic adsorption rate constants for Ca^{2+}, $Al(OH)_4^-$, and SO_4^{2-} (s^{-1}), respectively.

(b) Electric potential distribution between grains.

The Poisson equation was employed to characterize the distribution of the electric potential (ψ) between the cement grains [27]:

$$\nabla^2\psi = -\frac{F}{\varepsilon_r\varepsilon_0}\sum_k z_k c_k \quad k = Ca^{2+}, H_3SiO_4^-, Al(OH)_4^-, OH^-, SO_4^{2-} \tag{36}$$

(c) Heat transfer in paste.

During the initial stage, water adsorption, initial dissolution, and a fast reaction of C_3A occur immediately when the cement grains come into contact with water, resulting in heat generation within the cement paste [47,48]. The heat conduction equation can be utilized to determine the temperature distribution within the paste at the macroscale level, as follows [49]:

$$\rho_P C_P \dot{T} = \nabla(k_P \nabla T) + H_{C_3A}^V k_{ads} \exp(-k_{ads} t) \tag{37}$$

$$\rho_P = \frac{1 + w/c + m_{gypsum}\%}{\frac{1}{\rho_{cement}} + \frac{w/c}{\rho_{H_2O}} + \frac{m_{gypsum}\%}{\rho_{gypsum}}} \tag{38}$$

$$C_P = \frac{C_{cement} + w/c \cdot C_{H_2O} + m_{gypsum}\% \cdot C_{gypsum}}{1 + w/c + m_{gypsum}\%} \tag{39}$$

where ρ_P represents the density of the cement paste (kg m^{-3}). C_P, C_{cement}, C_{H_2O}, and C_{gypsum} denote the specific heat capacities of cement paste, cement, water, and gypsum (J kg^{-1} K^{-1}), respectively. k_P, $H_{C_3A}^V$, and k_{ads} are the thermal conductivity of the cement paste (W m^{-1} K^{-1}), enthalpy of heat release for the C_3A hydration reaction per unit volume (J m^{-3}), and ionic adsorption rate constant on the cement surface (s^{-1}), respectively.

The first and second terms on the right sides of Eq. (37) represent the heat flux and heat source owing to the initial dissolution of the clinker phases and the fast reaction of C_3A considering ionic adsorption. $H_{C_3A}^V$ is given by:

$$H_{C_3A}^V = \frac{H_{C_3A}}{SSA_{cement}} \times O_V^{B-cem} \tag{40}$$

where H_{C_3A} is the enthalpy of heat release for the C_3A hydration reaction per unit mass (J g^{-1}).

2.2. Kinetic shift from silicate- to aluminate-dominant

The hydration heat flow was calculated to determine the kinetic shift from silicate- to aluminate- dominant cement hydration, which was induced by multi-mineral reactions and interactions. It is generally believed that the hydration heat flow is dominated by silicate and aluminate phase reactions during the pre-induction, induction, acceleration, deceleration, and stabilization periods [2], as shown in Fig. 2. A literature review revealed that heat flow is usually calculated by empirical equations with numerical fitting instead of theoretical computations originating from the combination of dissolution, diffusion, precipitation, and adsorption behaviors during all hydration periods [20,50–52]. It may be difficult to determine the mechanism of the kinetic shift from silicate to aluminate dominance. To solve this issue, a novel cement hydration heat flow ($\dot{Q}$) formula is proposed that covers all periods without any fitting and without changing the parameters for each case. It was assumed that the $\dot{Q}$ during cement hydration was attributed to (i) an early-stage heat flow due to the initial dissolution of various clinker phases and the fast reaction of C_3A, and (ii) a later-stage heat flow resulting from the silicate and aluminate phase reactions in the cement clinker [47]. Thus, the $\dot{Q}$ is calculated as follows:

$$\dot{Q} = \dot{Q}_E + \dot{Q}_L \tag{41}$$

where

$$\dot{Q}_E = H_{C_3A} k_{ads} m_{gypsum}\% \frac{m_{C_3A}}{m_{C_3S}} \left[\exp\left(-w/c \cdot \frac{m_{C_3A}}{m_{gypsum}} k_{ads} t\right) + \exp(-E_{ads}^{C_3S}/E_a^{C_3A})\right] \tag{42}$$

$$\dot{Q}_L = \dot{Q}_L^{silicate} + \dot{Q}_L^{aluminate} \tag{43}$$

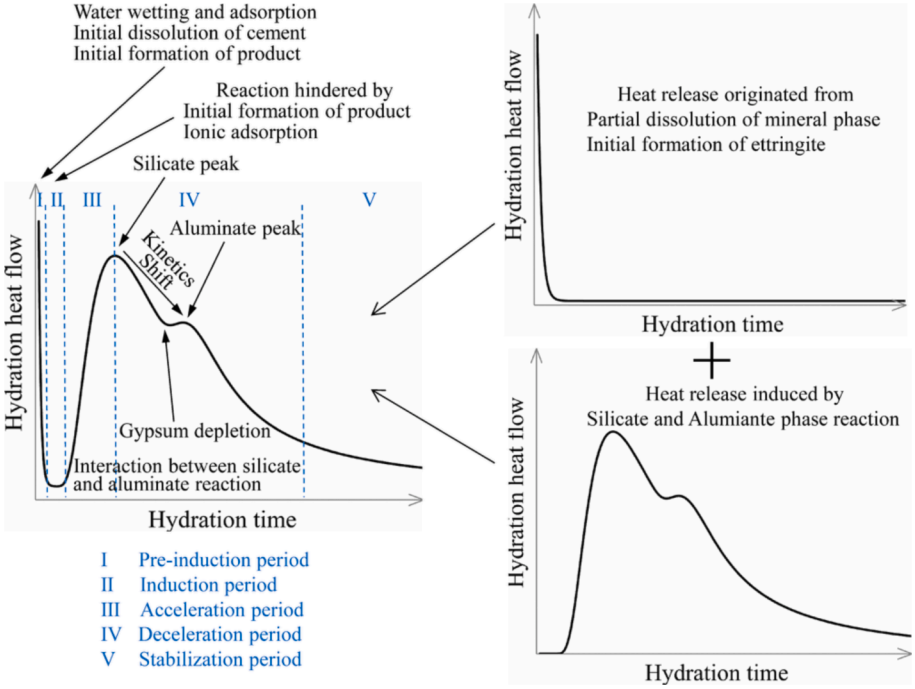

Fig. 2. A typical heat flow curve of Portland cement hydration.

$$\dot{Q}_L^{silicate} = \frac{m_{C_3S} w/c}{m_{C_2S} m_{gypsum} n_{clinker}} Q_{finite}^{silicate} (\beta_{silicate}/t)(\tau_{silicate}/t)^{\beta_{silicate}} \exp\Big(- (\tau_{silicate}/t)^{\beta_{silicate}} \Big) \quad (44)$$

$$\dot{Q}_L^{aluminate} = S_{C_3A} \frac{m_{other} w/c}{m_{gypsum}} Q_{finite}^{aluminate} (\beta_{aluminate}/t)(\tau_{aluminate}/t)^{\beta_{aluminate}} \exp\Big(- (\tau_{aluminate}/t)^{\beta_{aluminate}} \Big) \quad (45)$$

where H_{C_3A}, k_{ads}, m_{gypsum}, m_{C_3A}, m_{C_3S}, m_{C_2S}, m_{other}, $E_{ads}^{C_3S}$, $E_a^{C_3A}$, $n_{clinker}$, and S_{C_3A} denote the enthalpy of heat release for the C_3A hydration reaction (J g^{-1}), ionic adsorption rate constant on the C_3A surface (s^{-1}), gypsum content (%), C_3A content (%), C_3S content (%), C_2S content (%), other mineral content (%), adsorption energy of water on the C_3S grain surface per unit mass of C_3S (J mol^{-1}), activation energy for C_3A hydration (J mol^{-1}), number of main mineral types in PC, and exposed surface area fraction of C_3A on the cement grains, respectively. $\tau_{silicate}$, $\beta_{silicate}$, $\tau_{aluminate}$, and $\beta_{aluminate}$ represent the apparent time (s) and apparent energy ratio for the silicate and aluminate reactions, respectively. $Q_{finite}^{silicate}$ and $Q_{finite}^{aluminate}$ are the total cumulative heat for the silicate and aluminate reactions (J g^{-1}), respectively, which are given by

$$\tau_{silicate} = C_{C_3S-C_2S} w/c (m_{gypsum}/m_{C_3A})/(SSA_{cem} h_P (K_{C_3A}/K_{CSH})) \quad (46)$$

$$\beta_{silicate} = E_{ads}^{C_3S}/E_a^{C_3A} \quad (47)$$

$$Q_{finite}^{silicate} = H_{C_3S} SSA_{cem} \int_0^{t_{total}} \int_0^L v_{C_3S} d\xi dt + H_{C_2S} SSA_{cem} \int_0^{t_{total}} \int_0^L v_{C_2S} d\xi dt \quad (48)$$

$$\tau_{aluminate} = C_{C_3A} m_{gypsum} \big(K_{gypsum} K_{AFm}/K_{ettringite}\big)/(SSA_{cem} h_P) \quad (49)$$

$$\beta_{aluminate} = E_{ads}^{C_3S}/E_a^{C_2S} \quad (50)$$

$$Q_{finite}^{aluminate} = H_{C_3A}^{ettringite} n_{C_3A}^{ettringite} SSA_{cem} \int_0^{t_{total}} \int_0^L v_{AFt} d\xi dt + H_{C_3A}^{AFm} n_{C_3A}^{AFm} SSA_{cem} \int_0^{t_{total}} \int_0^L v_{AFm} d\xi dt \quad (51)$$

where h_P, $C_{C_3S-C_2S}$, C_{C_3A}, H_{C_3S}, H_{C_2S}, and $E_a^{C_2S}$ are the convective heat transfer coefficient (W m^{-2} K^{-1}), specific heat capacity of the silicate phase (J kg^{-1} K^{-1}), specific heat capacity of C_3A (J kg^{-1} K^{-1}), enthalpy of heat release for the C_3S hydration reaction (J mol^{-1}), enthalpy of heat release for the C_2S hydration reaction (J mol^{-1}), and activation energy for C_2S hydration (J mol^{-1}), respectively. $H_{C_3A}^{ettringite}$, $H_{C_3A}^{AFm}$, $n_{C_3A}^{ettringite}$, and $n_{C_3A}^{AFm}$ represent the heat of formation of ettringite per mole of C_3A (J mol^{-1}), heat of formation of AFm per mole of C_3A (J mol^{-1}), molar ratio of C_3A to AFt, and molar ratio of C_3A to AFm, respectively. The boundary and initial conditions for the governing equations are as follows.

Fig. 1 shows the Dirichlet-type boundary conditions imposed at the cement hydration paste edge to determine the temperature field.

$$T = T_M \quad \text{at} \quad r = \lambda \quad (52)$$

where T_M is the room temperature (K).

A boundary condition in the Neumann form is required at the symmetric center to describe the temperature field.

$$\frac{\partial T}{\partial r} = 0 \quad \text{at} \quad r = 0 \quad (53)$$

Fig. 1 shows the two Dirichlet boundary conditions imposed on the grain surface to describe the chemical and electrical fields.

$$c_{Ca^{2+}} = c_{Ca^{2+}}^e, c_{H_3SiO_4^-} = c_{H_3SiO_4^-}^e, c_{Al(OH)_4^-} = c_{Al(OH)_4^-}^e, c_{OH^-} = c_{OH^-}^e, c_{SO_4^{2-}} = 0, \psi = 0 \text{at} \xi = 0 \quad (54)$$

where c_k^e denotes the saturated concentration (mM) of the kth ionic species. Two boundary conditions in the Neumann form are required at the symmetric axis to describe the chemical and electric fields:

$$c_{Ca^{2+}} = c_{Ca^{2+}}^e, \frac{\partial c_{H_3SiO_4^-}}{\partial \xi} = 0, \frac{\partial c_{Al(OH)_4^-}}{\partial \xi} = 0, \frac{\partial c_{OH^-}}{\partial \xi} = 0, c_{SO_4^{2-}} = c_{SO_4^{2-}}^e, \frac{\partial \psi}{\partial \xi} = 0 \text{at} \xi = L \quad (55)$$

where $L = L_0 \left[\left(w/c \cdot \rho_{cem} \cdot \rho_{H_2O}^{-1} + 1 \right)^{1/3} - 1 \right]$ [53] is the distance between the C_3A and gypsum grain surfaces. The initial conditions for the temperature, chemical, and electric fields were as follows:

$$T = T_M, \; c_k = 0, \; \psi = 0 \quad at \quad t = 0 \quad (56)$$

Thus far, the multi-mineral reactive transport model has been formulated and numerically calculated using the flowchart shown in Fig. 3. To simplify the numerical computation, the governing equations were rewritten in a non-dimensional form by utilizing the definition of dimensionless parameters (Supporting Information).

3. Results and discussion

3.1. Model validation

The six comparisons between the presently theoretical simulation and published experimental results are conducted for heat flow $\dot{Q}$ under various mineral compositions, gypsum contents, curing temperatures, w/c ratios, SSAs, and mixing procedures [3,54–58], as shown in Fig. 4. The COMSOL Multiphysics software was used with the input parameters listed in Tables S1 and S2 (Supporting Information) for the governing coupled nonlinear partial differential equations. The values of the parameters used to validate the cement hydration reactions were obtained directly from the published experimental data. The global error (δ_G) for the time evolution $\dot{Q}$ was calculated [59], as well as the relative errors for peak heat flow (δ_{phf}) and peak heat time (δ_{pht}) [60].

For Cases (1)–(6), the global error (δ_G), relative errors for the peak heat flow (δ_{phf}), and peak heat time (δ_{pht}) are listed in Table 1. It was found that δ_G ranged from 12.92 to 23.16%, while δ_{phf} = 4.22–17.35% and δ_{pht} = 1.58–15.46% for the silicate phase peak, δ_{phf} = 2.26–20.41% and δ_{pht} = 1.11–13.00% for the aluminate phase peak. Considering the significant differences in mineral composition, gypsum content, curing temperature, w/c ratio, SSA, and mixing procedure for each case [3,54–58], the global and relative errors show satisfactory results for the present theoretical model to predict the heat flow for cement hydration. The errors between the experimental data and the simulation results may be due to several factors that were not considered in the model, such as the mixing procedure [61], pH [62], and moisture content [63]. This satisfactory agreement indicates that the present model can accurately predict cement hydration kinetics under various conditions. Moreover, the present model did not fit, and there was no need to

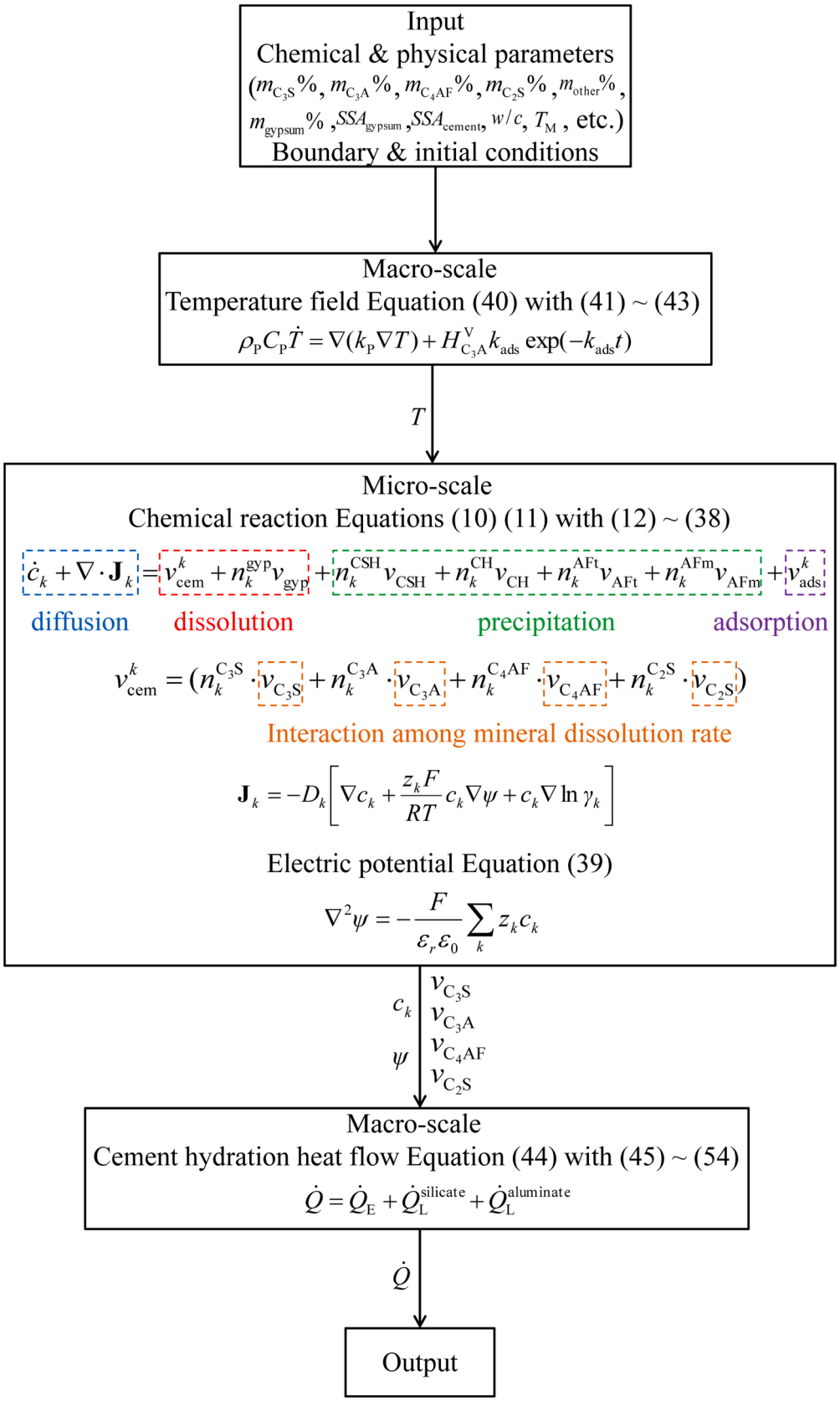

Fig. 3. Computational flowchart of the theoretical model.

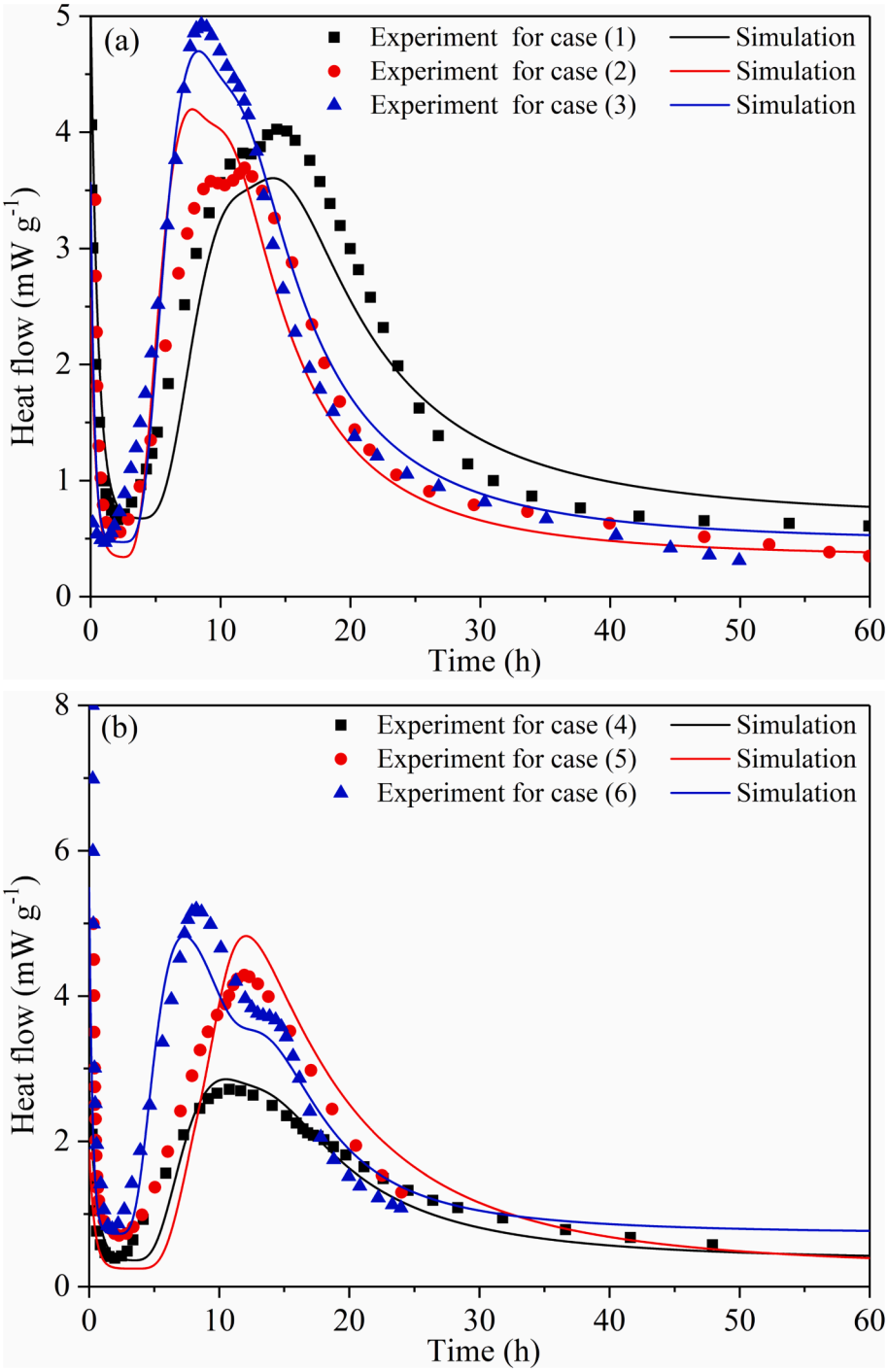

Fig. 4. Comparisons of heat flow $\dot{Q}$ between experimental data and simulation results under various mineral compositions, curing temperatures, w/c ratios, SSAs.

Table 1
The global and relative errors for all the comparisons.

Case	Reference	Mineral composition of cement (mass%)				Global error (%)	Relative error (%)			
							Silicate peak		Aluminate peak	
		C_3S	C_3A	C_4AF	C_2S	δ_G	δ_{phf}	δ_{pht}	δ_{phf}	δ_{pht}
(1)	[54]	58.73	6.84	10.91	15.51	18.85	7.64	3.83	10.45	2.10
(2)	[55]	61.78	6.44	9.58	11.58	18.47	17.35	15.46	4.45	7.24
(3)	[56]	60.36	8.04	8.35	11.38	13.73	4.66	2.50	2.26	2.10
(4)	[3]	74.15	6.18	8.1	5.79	12.92	5.09	2.42	20.41	13.00
(5)	[57]	68.2	5.1	11.4	7.1	23.16	4.22	1.58	12.54	1.11
(6)	[58]	57.7	10.4	1.9	19.7	13.90	7.06	11.03	6.52	4.42

change the parameters for each case. Indeed, the polymorphs of C_3A affect its hydration. A literature search reveals that the hydration kinetics of cubic and orthorhombic C_3A has been experimentally investigated, which showed different reaction rates and products [64,65]. Moreover, the C_3A dissolution rate constant has different values for different polymorphs of C_3A [66]. Usually, the C_3A crystal structure is determined at the nanometer scale [64,66,67]. However, the present model only considers the cement particle at microscale level with spherical shape. To quantify the relationship between C_3A crystal and dissolution kinetics, a molecular dynamic simulation may be required.

Fig. 4 shows that the occurrence times observed for the main hydration peak (silicate peak) and the exothermic shoulder peak (aluminate peak) were different when subjected to the different mineral compositions used in these experimental cases, particularly the C_3S, C_3A, and gypsum contents. Moreover, the value of the silicate peak was higher than that of the aluminate peak in cases (3) [56] and (4) [3], while the aluminate peak was higher than the silicate peak in cases (1) [54], (2) [55], and (5) [57], which may be attributed to the C_3S-to-C_3A content ratio and gypsum content. In addition, the SSA of the cement grains significantly affected the silicate and aluminate peak values and occurrence times. This indicates that the interactions between the silicate and aluminate reactions are key to controlling the hydration kinetics, shifting the silicate phase reaction to the aluminate phase reaction as the dominant reaction. Further details are presented in the following section.

3.2. Combined effect of dissolution, precipitation, diffusion, and adsorption

Generally, interactions among mineral phases are achieved through dissolution-precipitation-diffusion-adsorption coupled behavior during cement hydration [2]. In this subsection, the effects of dissolution, diffusion, precipitation, and adsorption behaviors on the cement hydration kinetics shifting from silicate to aluminate were studied individually and in combination. The input parameters are listed in Tables S1 and S3 (Supporting Information).

3.2.1. Effect of dissolution and precipitation behaviors

For cement hydration, dissolution and precipitation are the processes that produce and consume ionic species, respectively, which determine the concentration of the ionic species and control the hydration reaction kinetics. Therefore, the effects of dissolution and precipitation on cement hydration were investigated using the proposed model.

The C_3A solubility constant (K_{C_3A}) represents the solubility product in the equilibrium state and plays an important role as the driving force of C_3A dissolution [68]. Thus, $\dot{Q}$ was studied using the proposed model, with $K_{C_3A} = 0.8 \times 10^{-20.65}$, $10^{-20.65}$, and $1.2 \times 10^{-20.65}$, respectively. Fig. 5 shows that the main hydration peak (silicate peak) significantly increased from 3.0 to 4.4 mW•g^{-1} and the occurrence time of the silicate peak decreased from 10.5 to 7.9 h; the exothermic shoulder peak (aluminate peak) and occurrence time of the aluminate peak showed slight differences when K_{C_3A} increased from $0.8 \times 10^{-20.65}$ to $1.2 \times 10^{-20.65}$. This may be attributed to the increased K_{C_3A}, resulting in a higher degree of undersaturation in C_3A, leading to faster dissolution of C_3A and formation of ettringite accompanied by the consumption of sulfate ions, promoting the dissolution of gypsum and release of sulfate ions in the cement paste, which enhanced the adsorption of sulfate on the C-S-H surface and accelerated the C_3S hydration reaction [10].

Fig. 6 shows the plots of $\dot{Q}$ when K_{gypsum} was set at $0.9 \times 10^{-4.58}$, $10^{-4.58}$, and $1.1 \times 10^{-4.58}$, respectively. The aluminate peak significantly decreases from 3.9 to 3.2 mW•g^{-1} and the occurrence time of the aluminate peak increases from 11.4 to 14.3 h when K_{gypsum} was increased from $0.9 \times 10^{-4.58}$ to $1.1 \times 10^{-4.58}$. In this case, increasing K_{gypsum} increases the degree of undersaturation in gypsum, which strengthens the driving force for gypsum dissolution. Therefore, the retarding effect of gypsum on the hydration of C_3A was enhanced by the higher gypsum dissolution rate, which decreased the aluminate reaction peak and increased the occurrence time of the aluminate peak [69]. The faster dissolution of gypsum resulted in a longer time interval between the silicate and aluminate peaks.

For C_3S dissolution, the initial stage of the reaction between C_3S with water is an incongruent dissolution associated with the formation of a silica-rich layer on the surface of C_3S. Due to the characteristic structure

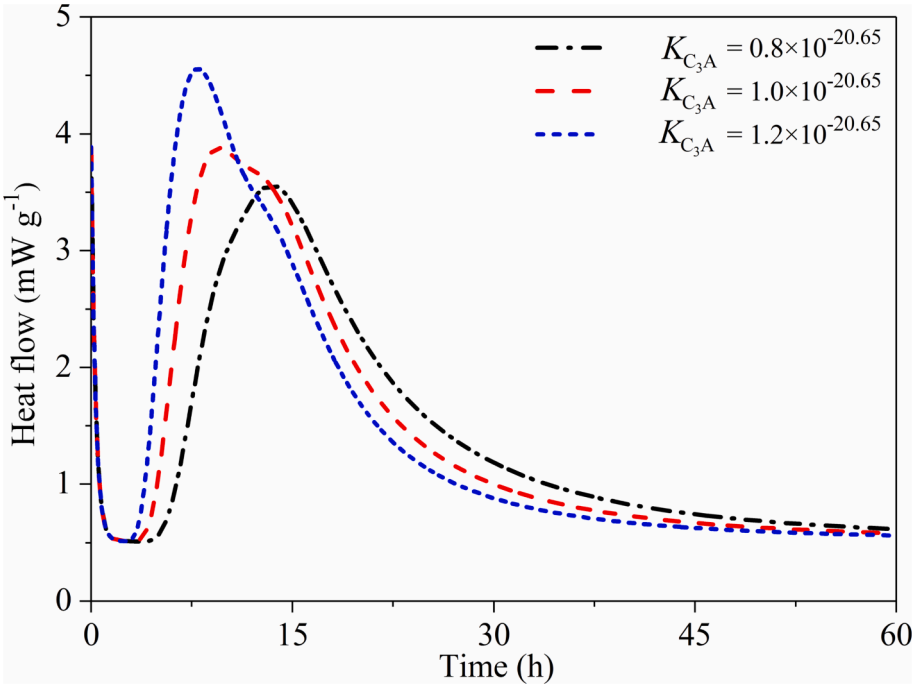

Fig. 5. Effect of C_3A solubility constant K_{C_3A} on hydration heat flow $\dot{Q}$.

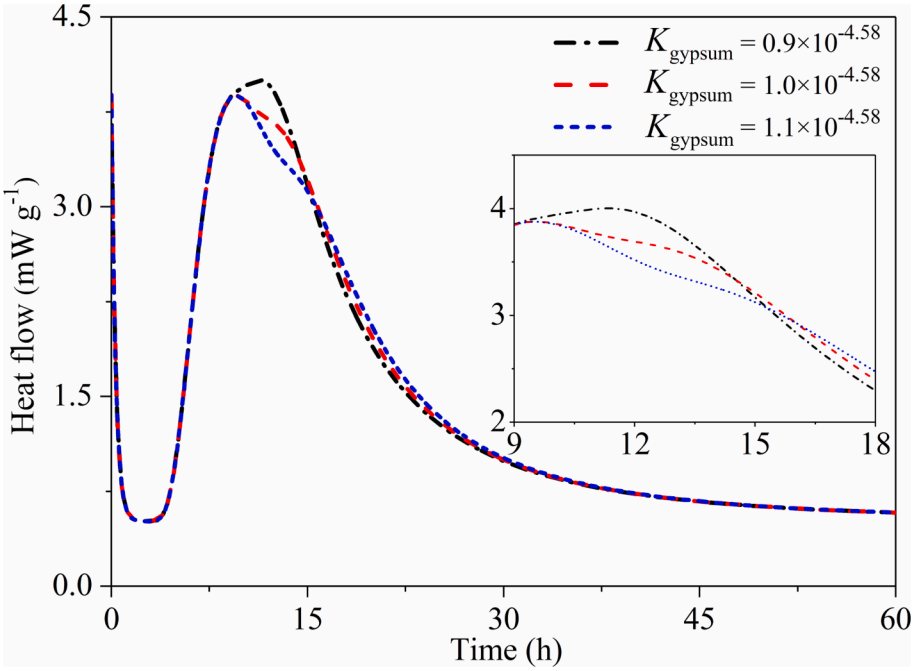

Fig. 6. Effect of gypsum solubility constant K_{gypsum} on hydration heat flow $\dot{Q}$.

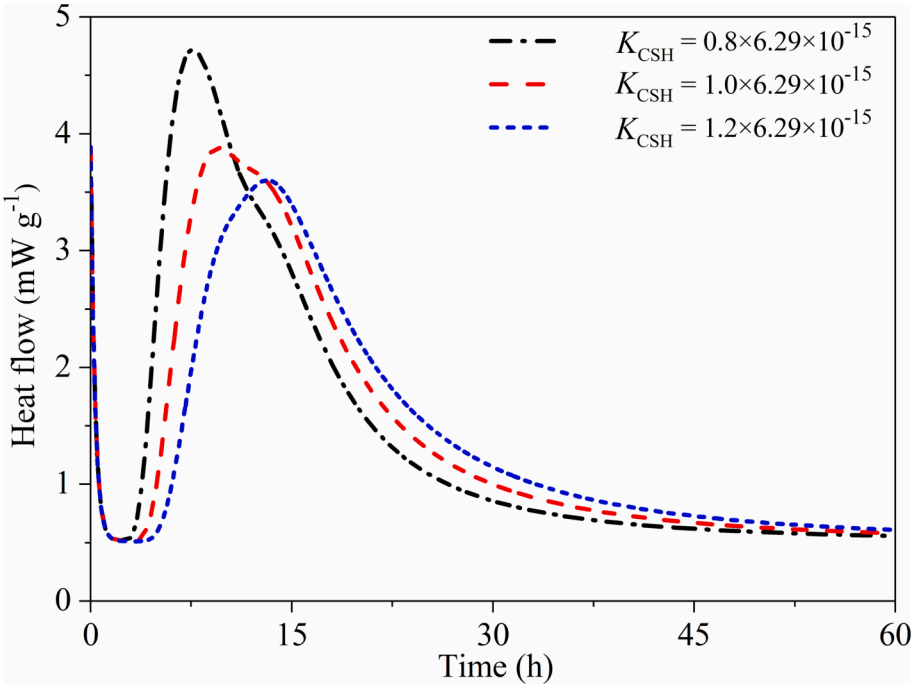

Fig. 7. Effect of C-S-H solubility constant K_{CSH} on hydration heat flow $\dot{Q}$.

of C_3S, the calcium ions dissolve faster than silicate ions [70]. During the initial stage of C_3S hydration, the ratio of calcium and silicate concentration (Ca/Si) in the pore solution was almost 800 ~ 1000 when the water/solid (w/c) ratio was a normal value, such as 0.4 and 0.5 [71–75]. Although several experiment results showed that the Ca/Si ratio in pore solution was close to 3, the w/c ratios in these experiments were very high, such as 200 and 10,000 [23,76]. Moreover, the experiments also indicated that the Ca/Si ratio decreased from 2000 to 3 when the w/c ratio increased from 0.5 to 200 [70]. The high water content promotes the C_3S dissolution and C-S-H precipitation and encourages higher silicate concentration [23,77], which results in Ca/Si ratio close to 3 in the pore solution. Thus, the Ca/Si ratio under the high w/c ratio can not serve as evidence of congruent dissolution during the initial stage of the reaction between C_3S with water.

In addition to clinker phase dissolution, the precipitation of hydration products is also a key driver of the cement hydration reaction. With respect to the silicate reaction, C-S-H precipitation played an important role in the cement hydration reaction kinetics. Thus, $\dot{Q}$ was studied when K_{CSH} was set to $0.8 \times 6.29 \times 10^{-15}$, 6.29×10^{-15}, and $1.2 \times 6.29 \times 10^{-15}$. Fig. 7 shows the silicate peak increased from 3.2 to 4.7 mW•g^{-1}

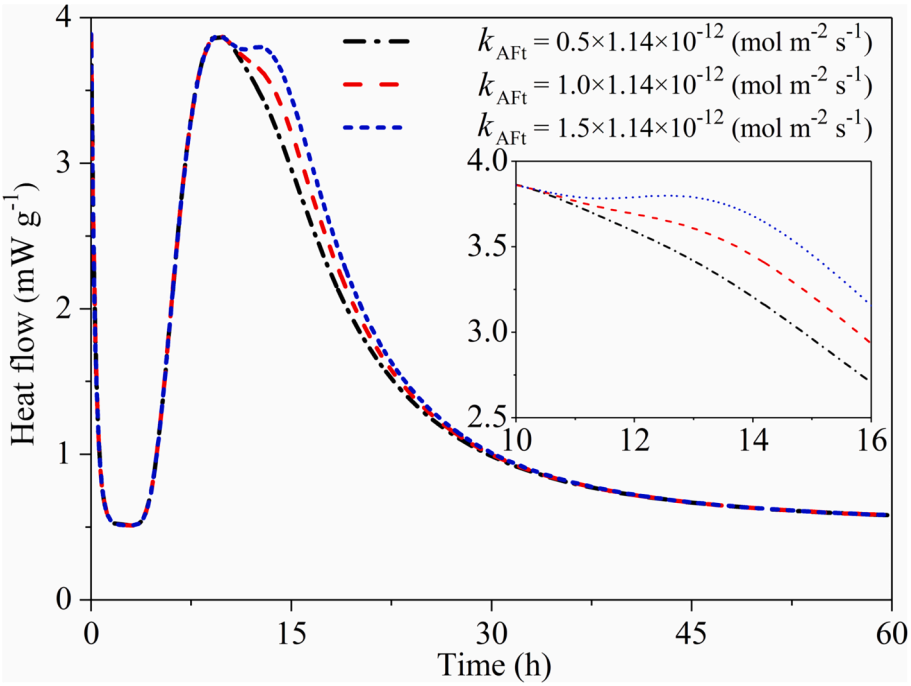

Fig. 8. Effect of ettringite precipitation rate constant k_{AFt} on hydration heat flow $\dot{Q}$.

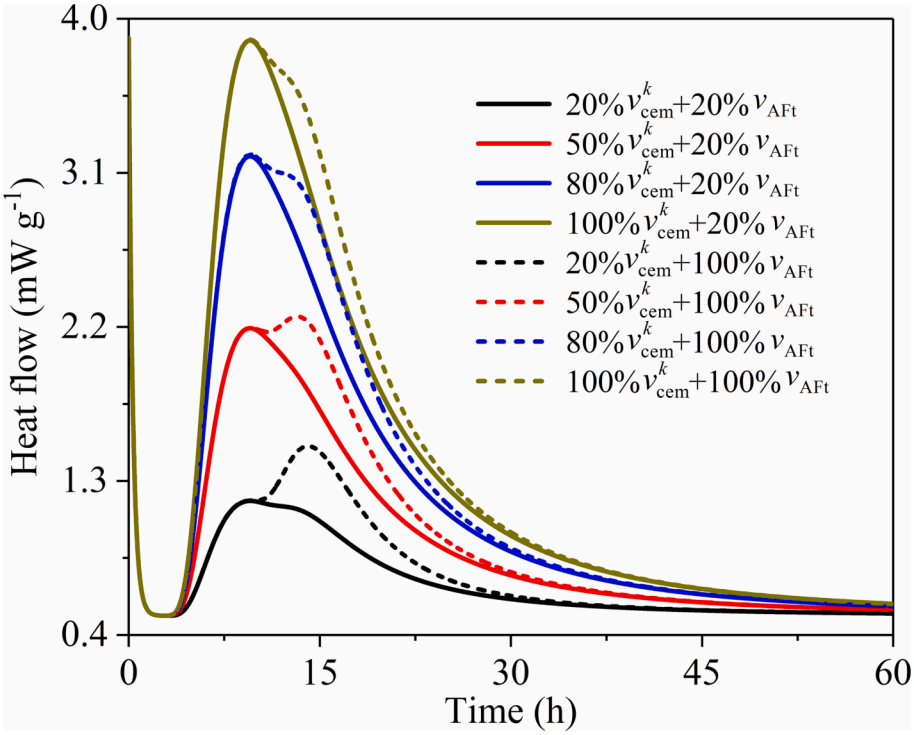

Fig. 9. Combined effect of dissolution and precipitation on hydration kinetics under different cement dissolution rates v^k_{cem}.

and the occurrence time of the silicate peak decreased from 10.1 to 7.6 h when K_{CSH} decreased from 1.2 × 6.29 × 10^{-15} to 0.8 × 6.29 × 10^{-15}, which can be attributed to the decreased K_{CSH} leading to a higher degree of supersaturation in C-S-H, which promotes the silicate reaction. With K_{CSH} decreasing from 1.2 × 6.29 × 10^{-15} to 0.8 × 6.29 × 10^{-15}, the aluminate peak decreased from 3.6 to 3.4 mW•g^{-1} and the occurrence time of the aluminate peak decreased from 13.6 to 12.5 h. It was concluded that faster precipitation of C-S-H resulted in a larger difference between the silicate and aluminate peak values and times.

Furthermore, the effect of ettringite precipitation on cement hydration is an important aspect of the aluminate reaction. The aluminate peak was studied when k_{AFt} was set to 0.5 × 1.14 × 10^{-12}, 1.14 × 10^{-12}, and 1.5 × 1.14 × 10^{-12} mol•m^{-2} s^{-1}. Fig. 8 shows the aluminate peak significantly increased from 3.4 to 3.7 mW•g^{-1} when k_{AFt} increases from 0.5 × 1.14 × 10^{-12} to 1.5 × 1.14 × 10^{-12} mol•m^{-2} s^{-1}. This may be attributed to a larger k_{AFt} value, which leads to faster ettringite formation, resulting in a higher aluminate peak. It was also confirmed that the exothermic shoulder peak was controlled by the aluminate phase reaction.

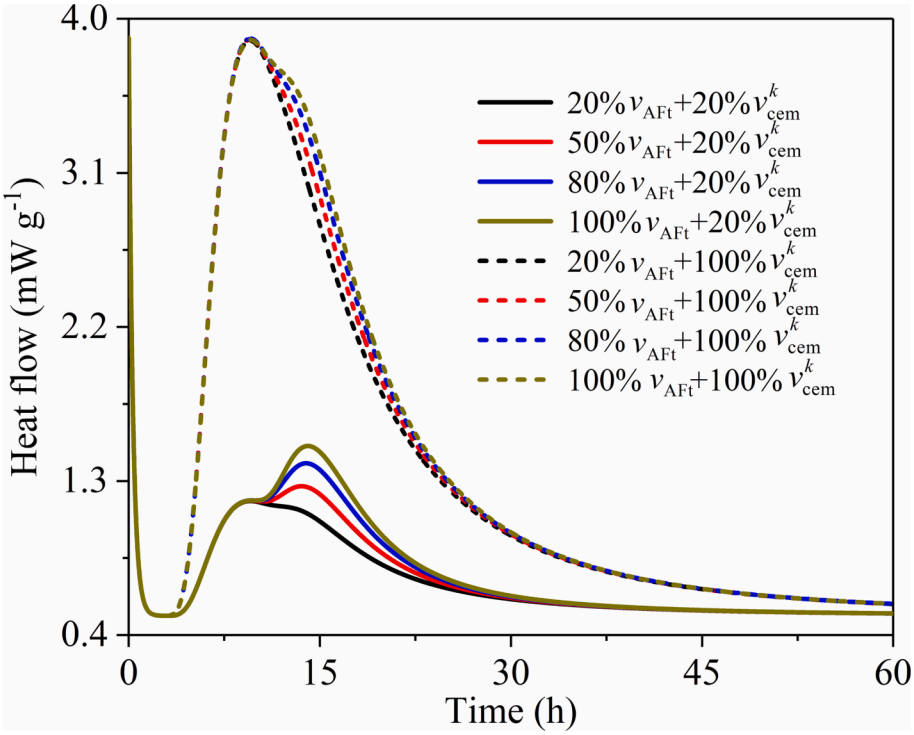

Fig. 10. Combined effect of dissolution and precipitation on hydration kinetics under different ettringite precipitation rates v_{AFt}.

To determine the combined effect of the dissolution and precipitation behaviors on the cement hydration kinetics, the time evolution of the hydration heat flow was analyzed using a model under various cement dissolution rates (v^k_{cem}) and ettringite precipitation rates (v_{AFt}). These two parameters are highly correlated with dissolution and precipitation kinetics, respectively. As shown in Fig. 9, quantitative analysis was carried out for the hydration heat flow with cement dissolution rates of 20%, 50%, 80%, and 100% v^k_{cem} when the ettringite precipitation rate was set to 20% and 100% v_{AFt}, respectively. It was observed that a faster rate of cement dissolution and ettringite precipitation led to higher silicate and aluminate peaks. It was also found that the promotion effect of ettringite precipitation on the aluminate peak is more significant with a lower cement dissolution rate during cement hydration. Correspondingly, Fig. 10 shows the time evolution of the heat flow with ettringite precipitation rates of 20%, 50%, 80%, and 100% v_{AFt} when the cement dissolution rate was set to 20% and 100% v^k_{cem}, respectively. This also confirmed the promotion effect of cement dissolution and ettringite

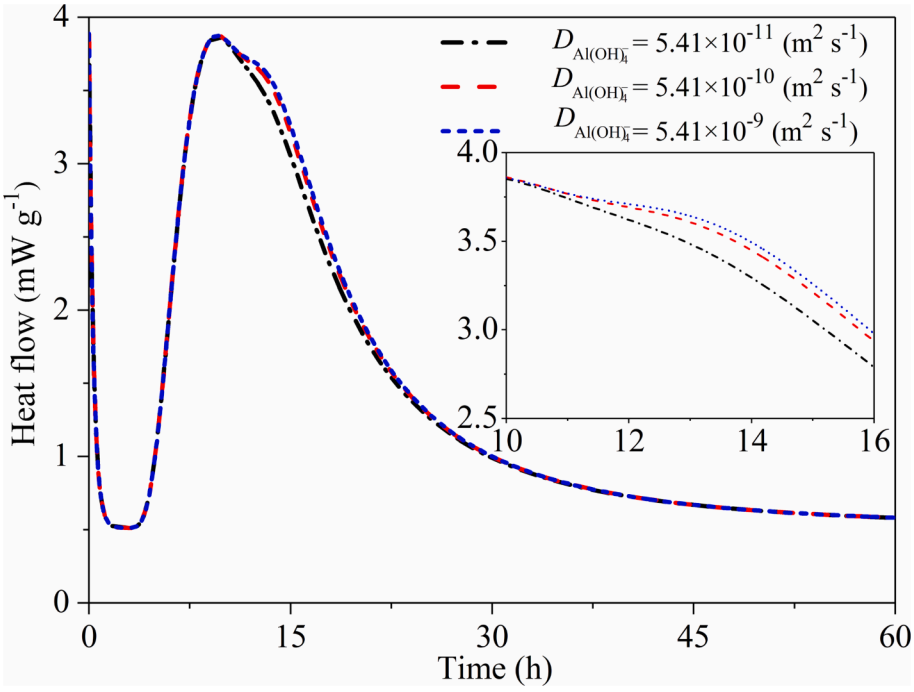

Fig. 11. Effect of aluminum ion diffusion coefficient $D_{Al(OH)_4^-}$ on hydration heat flow $\dot{Q}$.

precipitation on the hydration heat flow. A comparison of Fig. 9 with Fig. 10 suggests that cement dissolution has a more significant impact on the silicate peak, while ettringite precipitation had a more significant effect on the aluminate peak.

3.2.2. Effect of diffusion and adsorption behaviors

In addition to clinker phase dissolution and hydration product precipitation, ion diffusion and adsorption behavior have been proposed as mechanisms responsible for the cement hydration reaction rate. Therefore, the effects of diffusion and adsorption on cement hydration reaction kinetics were studied using the proposed model.

Generally, aluminum ions have a lower intrinsic diffusion coefficient in water than calcium, sulfate, or hydroxide ions [17]. The aluminum ion diffusion behavior determines the ettringite formation rate for the aluminate phase reaction and simultaneously affects the C_3S hydration reaction kinetics for the silicate phase reaction. Thus, $\dot{Q}$ was studied when the diffusion coefficient of aluminum ions ($D_{Al(OH)_4^-}$) was set to 5.41×10^{-11}, 5.41×10^{-10}, and 5.41×10^{-9} m^2s^{-1}, respectively. Fig. 11 shows the aluminate peak has slightly increased from 3.3 to 3.5 $mW \bullet g^{-1}$ upon increasing $D_{Al(OH)_4^-}$, which may be attributed to the faster ion diffusion optimizing the distribution of aluminum ions in cement paste, accelerating the reaction with gypsum to form ettringite. In addition, the slight effect of the aluminum ion diffusion coefficient indicates that ionic diffusion is not the main mechanism controlling the aluminate phase reaction.

It is well known that the adsorption behavior of ionic species on the surfaces of silicate and aluminate phases is a critical controlling factor affecting the reaction rate, which can explain the inhibition or promotion of cement hydration reaction kinetics. Therefore, the effect of adsorption on hydration heat flow was investigated to reveal the hydration mechanism using our model. In the present model, the term for the aluminum inhibition effect ($\frac{K_f^{C_3S-Al(OH)_4^-}}{K_f^{C_3S-Al(OH)_4^-}+\alpha_{Al(OH)_4^-}}$) is shown within the equation of the C_3S dissolution rate (Eq. (13)), which represents the inhibitory effect of aluminum on the C_3S dissolution rate. Hence, $\dot{Q}$ was performed using the C_3S dissolution rate equation with and without the aluminum inhibition term. Fig. 12 shows the silicate peak increased from 3.7 to 4.3 $mW \bullet g^{-1}$and the aluminate peak increased from 3.5 to 4.0 $mW \bullet g^{-1}$ when the aluminum inhibition term was removed from the C_3S dissolution rate equation. This may be attributed to the improved cement hydration rate when the inhibitory effect of aluminum on C_3S dissolution is not considered during the cement hydration reaction. This indicated that a quantitative analysis of the cement hydration reaction kinetics was achieved by combining adsorption and dissolution in the equation.

Additionally, the ionic species in the solution are consumed by adsorption, which has an important effect on dissolution, precipitation, and diffusion during the cement hydration reaction. Therefore, Fig. 13 shows the plot of $\dot{Q}$ when the aluminum ion adsorption rate constant ($k_{ads}^{Al(OH)_4^-}$) was set to 1/1617.9, 1/1217.9, and 1/817.9 s^{-1}, respectively. It can be seen that the silicate peak showed an obvious increase from 3.6 to 4.0 $mW \bullet g^{-1}$ and the aluminate peak increased from 3.3 to 3.8 $mW \bullet g^{-1}$ when $k_{ads}^{Al(OH)_4^-}$ increased from 1/1617.9 to 1/817.9 s^{-1}, which may be attributed to the faster aluminum ion adsorption rate promoting the removal of aluminum ions from the solution. This enhances the degree of undersaturation and thus, accelerates the diffusion and dissolution reactions.

Furthermore, the combined effect of diffusion and adsorption behaviors was investigated using a model for cement hydration kinetics under various diffusion coefficients ($D_{Al(OH)_4^-}$) and adsorption rate constants ($k_{ads}^{Al(OH)_4^-}$) for aluminum ions. These two parameters are strongly correlated with diffusion and adsorption kinetics, respectively. Fig. 14 presents the time evolution of the hydration heat flow with aluminum ion diffusion coefficients of 20%, 50%, 120%, and 200% $D_{Al(OH)_4^-}$ when the aluminum ion adsorption rate constant was set to 100% and 200% $k_{ads}^{Al(OH)_4^-}$, respectively. The promotion effect of aluminum ion diffusion on the aluminate peak was more significant with a higher adsorption rate of aluminum during cement hydration. In Fig. 15, the effect of ion adsorption on the time evolution of the heat flow under various adsorption rate constants with two different diffusion coefficients of aluminum is plotted. A comparison of Fig. 14 with Fig. 15 indicates that aluminum ion adsorption has a more significant influence on cement hydration kinetics than aluminum ion diffusion.

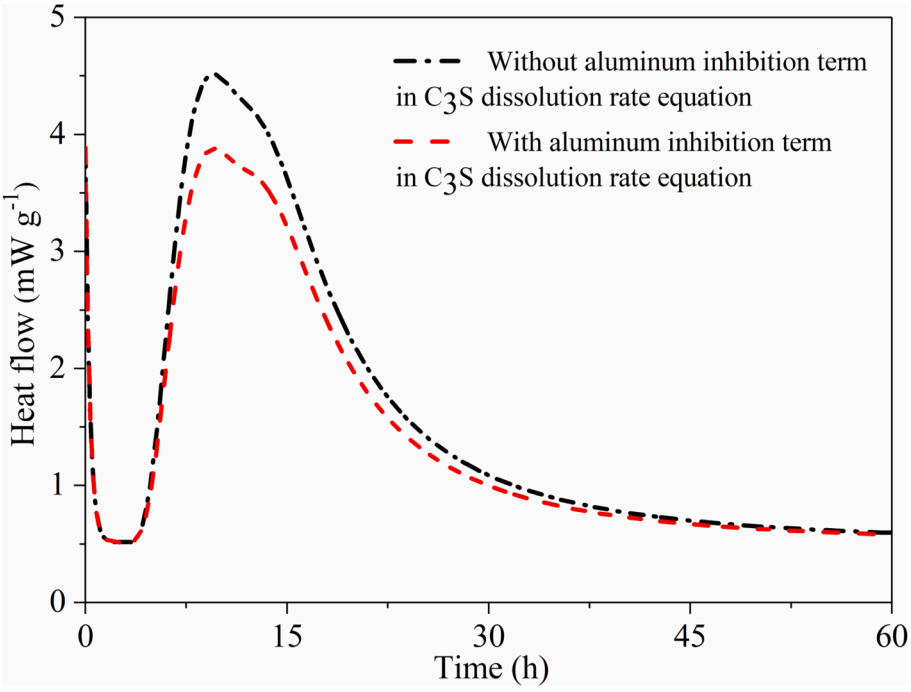

Fig. 12. Hydration heat flow $\dot{Q}$ with and without thealuminum inhibition term in C_3S dissolution rate equation.

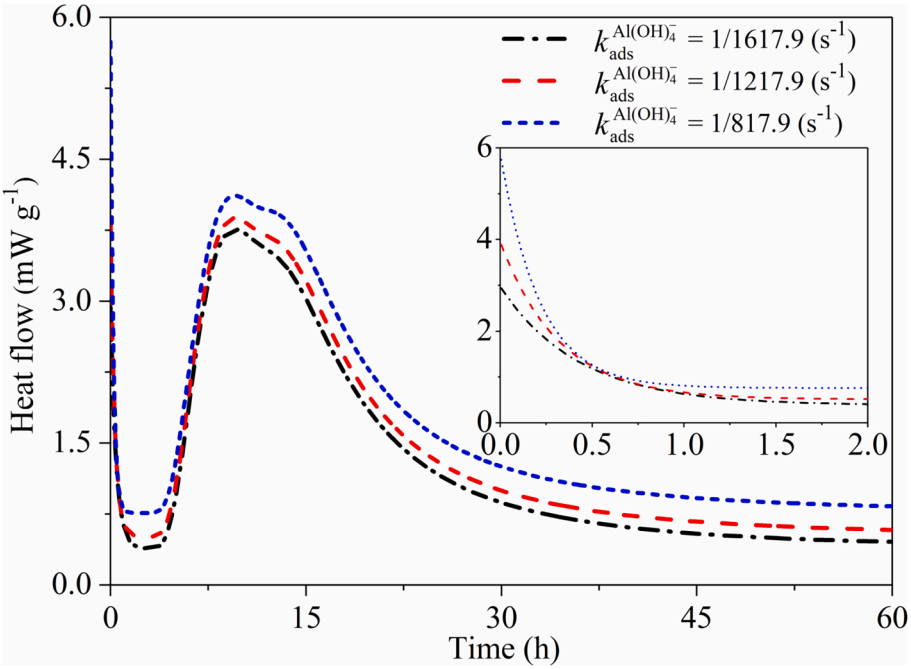

Fig. 13. Effect of aluminum adsorption rate constant $k_{ads}^{Al(OH)_4^-}$ on hydration heat flow $\dot{Q}$.

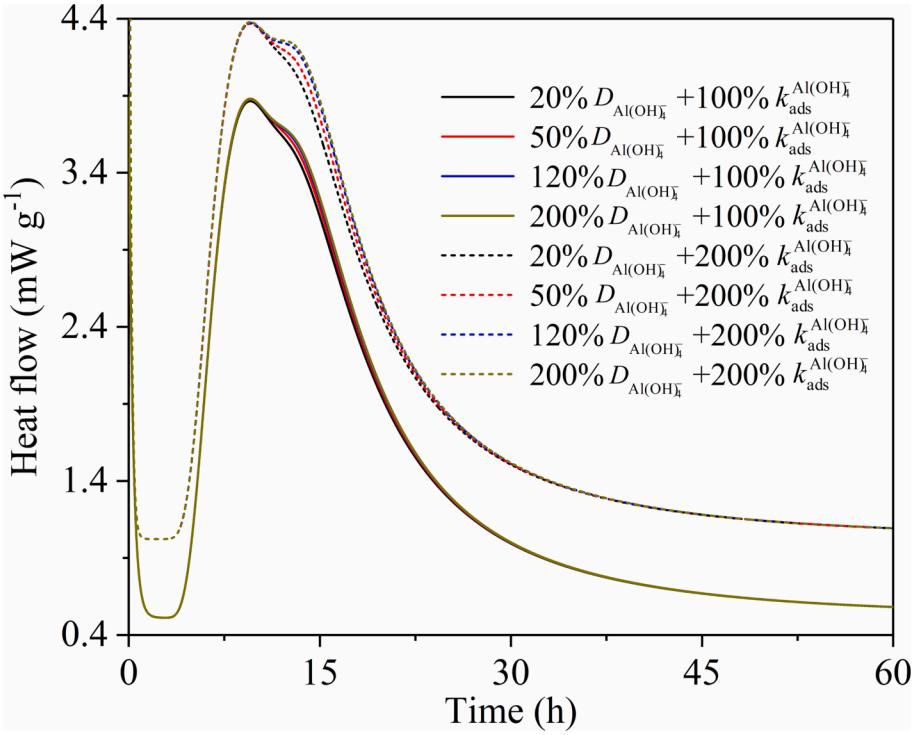

Fig. 14. Combined effect of diffusion and adsorption on hydration kinetics under different aluminum ion diffusion coefficients $D_{Al(OH)_4^-}$.

3.2.3. *Combined effect on hydration kinetics*

From the above discussion, it can be seen that the dissolution, precipitation, diffusion, and adsorption behaviors have individual effects on the cement hydration reaction kinetics. In light of previous findings, the driving force for clinker phase dissolution and hydration product precipitation was the degree of undersaturation and supersaturation in the solution, respectively, which are linked via the spatial and temporal distribution of ionic species in the solution controlled by diffusion and adsorption behavior [2,47]. Diffusion and adsorption result from the release of ionic species upon dissolution and are consumed during precipitation. Thus, the cement hydration kinetics are controlled by the combined effects of dissolution, precipitation, diffusion, adsorption, and interactions. The combined effects of the silicate and aluminate phase reactions are discussed below.

In terms of the silicate phase reaction, the combined effect was studied using the silicate peak observed during the evolution $\dot{Q}$. Fig. 11 and Fig. 12 indicate that $D_{Al(OH)_4^-}$ has a slight effect on the silicate peak

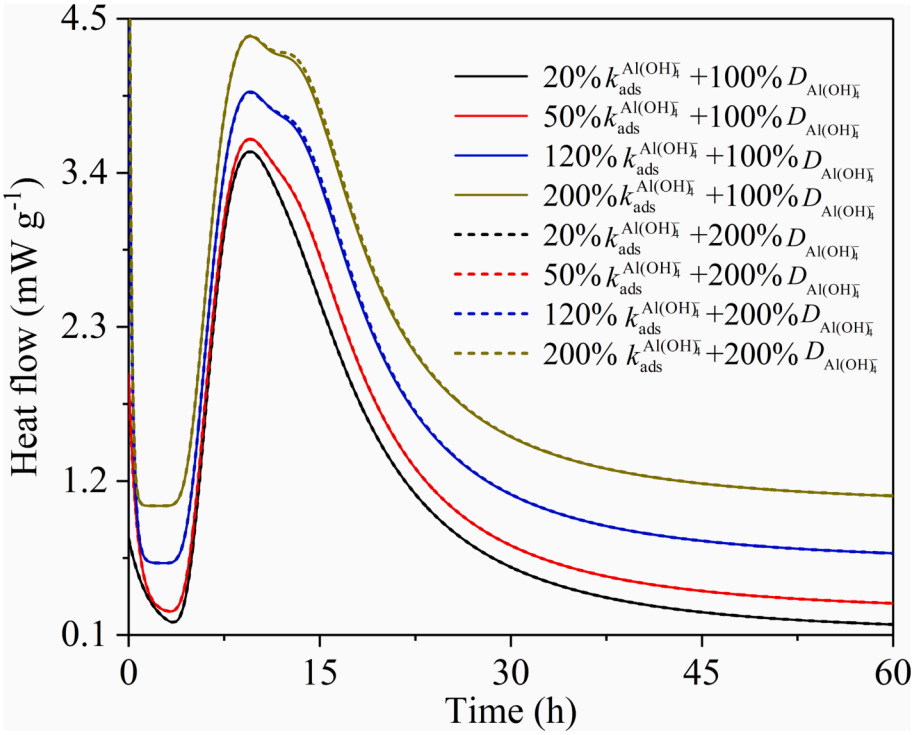

Fig. 15. Combined effect of diffusion and adsorption on hydration kinetics under different aluminum ion adsorption rate constants $k_{ads}^{Al(OH)_4^-}$.

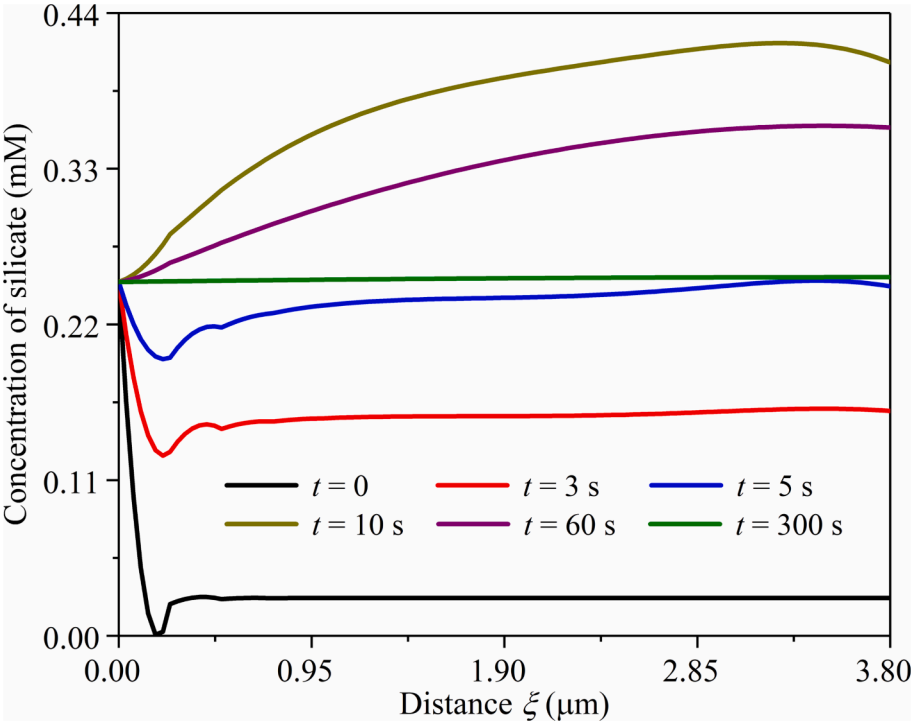

Fig. 16. The spatial distribution of silicate concentration when $K_{gypsum} = 10^{-4.58}$.

compared to the aluminum inhibitory effect ($\frac{K_f^{C_3S-Al(OH)_4^-}}{K_f^{C_3S-Al(OH)_4^-}+\alpha_{Al(OH)_4^-}}$) in the C_3S dissolution rate equation, which indicates that the diffusion of the ionic species was not the intrinsic mechanism hindering the C_3S reaction during the hydration reaction of cement. In addition, the spatial distribution of the ionic concentration can reveal the kinetics of the silicate phase reaction from the perspective of the release and consumption of ionic species. Fig. 16 shows a plot of the spatial distribution of the silicate concentration when $K_{gypsum} = 10^{-4.58}$. The silicate ions diffused from the cement grain surface ($\xi = 0$) to the gypsum grain surface ($\xi = 3.8$) when they were released from the cement grain surface owing to cement grain dissolution.

As time increased, the silicate ions on the gypsum grain surface ($\xi =$

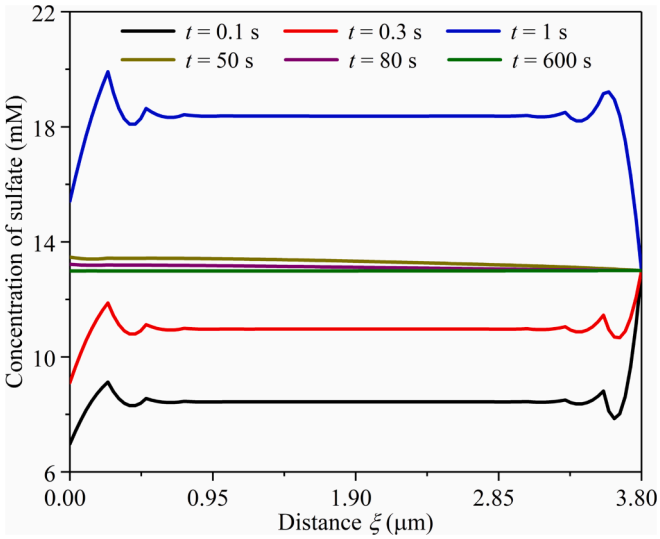

Fig. 17. The spatial distribution of sulfate concentration when $K_{gypsum} = 0.9 \times 10^{-4.58}$.

3.8) increased from zero to supersaturation and then decreased from supersaturation to saturation. This indicates that the minimum silicate concentration was observed near the cement grain surface ($\xi = 0.18$), which may have been due to the consumption of silicate ions induced by the precipitation of C-S-H around the cement grains. Moreover, the C-S-H solubility constant (K_{CSH}) had no effect on the spatial distribution of the silicate concentration during the first five minutes of the reaction. This demonstrates that the formation of the protective layer was not the main reason for the C_3S reaction retardation, but rather the adsorption of ionic species on the grain surface [4].

The aluminate peak was investigated with respect to aluminate phase reactions under various conditions. Fig. 5 and Fig. 8 show that the C_3A solubility constant (K_{C_3A}) and ettringite precipitation rate constant (k_{AFt}) have a significant effect on the aluminate peak, while the aluminum ion diffusion coefficient has a slight effect on the aluminate peak. This suggests that the aluminate phase reaction kinetics were controlled by a combination of C_3A dissolution and ettringite precipitation. Furthermore, Fig. 17 and Fig. 18 show the plots of the spatial distribution of the sulfate concentration when the gypsum solubility constant (K_{gypsum}) was $0.9 \times 10^{-4.58}$ and $1.1 \times 10^{-4.58}$, respectively. Sulfate ions diffused from the gypsum grain surface ($\xi = 3.8$) to the cement grain surface ($\xi = 0$). During the first 10 min, the sulfate ions at the cement grain surface ($\xi = 0$) increased from zero to the supersaturation concentration and then decreased from the supersaturation to the saturation concentration. Comparing Fig. 17 with Fig. 18, a higher sulfate concentration and the same saturation concentration were observed during the first 10 min when K_{gypsum} increased from $0.9 \times 10^{-4.58}$ to $1.1 \times 10^{-4.58}$, which demonstrates that more sulfate ions were consumed when $K_{gypsum} = 1.1 \times 10^{-4.58}$. Comparing Fig. 18 with Fig. 6, the increased sulfate consumption led to a lower aluminate peak. This indicates that the adsorption of calcium-sulfate ion-pair complexes reduced the number of active sites on the C_3A surface, inhibiting C_3A dissolution during the pre-induction and induction periods [78].

3.3. Kinetics shift under different mineral compositions

Based on the combined effects discussed in the previous subsection, the shift in cement hydration kinetics was studied for different mineral compositions. The main mineral phases of the PC were C_3S, C_3A, C_4AF, C_2S, and gypsum. Numerous studies have been conducted on pure C_3S, C_3A, C_4AF, and C_2S to understand their hydration reaction mechanisms [4–8]. Moreover, the hydration reactions of C_3S-C_3A, C_3S-C_4AF, C_3A-C_4AF, and C_3S-C_2S mixtures were also investigated to reveal the interaction between pure minerals using models and experiments [10,47,79,80]. Furthermore, the C_3S-C_3A-C_4AF-C_2S-gypsum system was also studied by simply summing the individual hydration reactions in several models [20,50,51,81], whereas there is a lack of sufficient understanding of the effect of different mineral compositions on hydration kinetic shifting from silicate- to aluminate-dominant. Thus, this

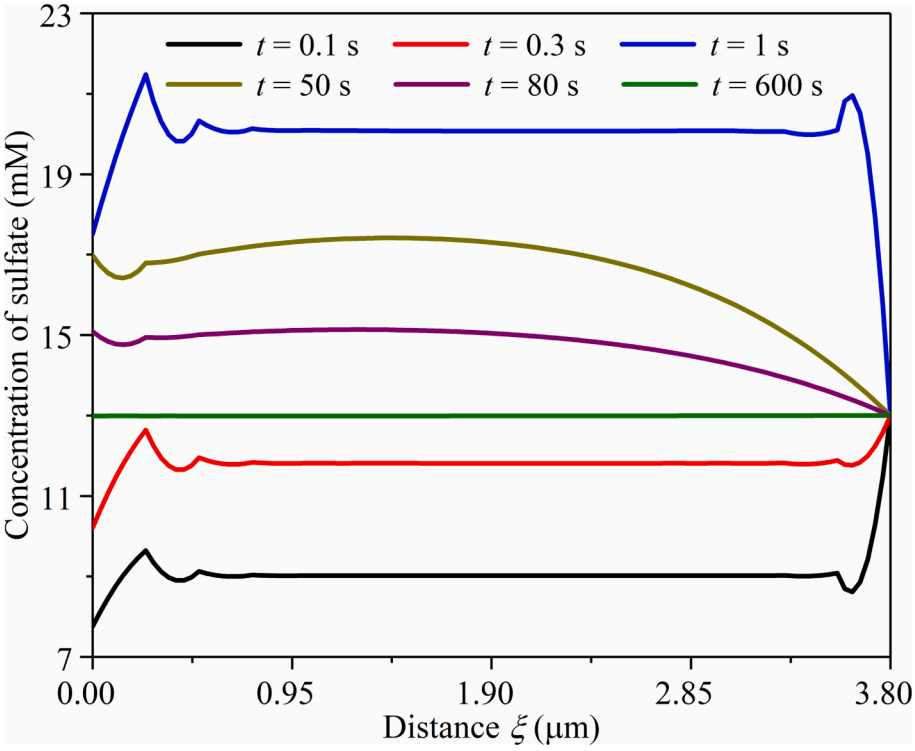

Fig. 18. The spatial distribution of sulfate concentration when $K_{gypsum} = 1.1 \times 10^{-4.58}$.

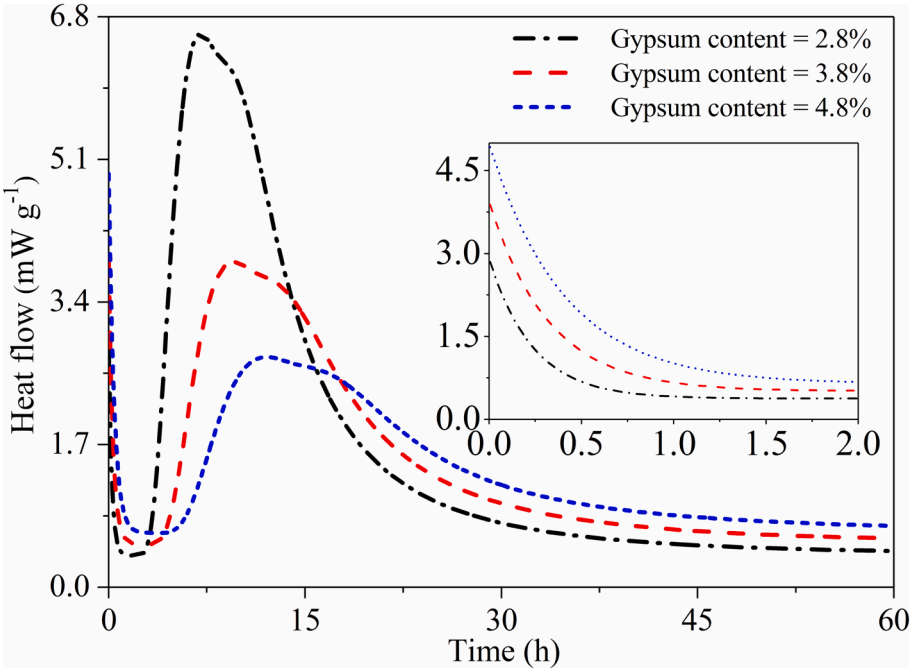

Fig. 19. Effect of gypsum content on hydration heat flow $\dot{Q}$.

subsection investigates the effect of mineral composition on the kinetic shift from silicate to aluminate dominant for cement hydration. The input parameters are listed in Tables S1 and S3 (Supporting Information).

3.3.1. Effect of gypsum content on kinetics shift

In general, gypsum plays an important role in cement hydration reaction kinetics and can be studied using the hydration heat flow. Indeed, many studies have focused on the effect of gypsum content on the hydration reaction kinetics of pure C_3S, C_3A, and C_3S/C_3A systems and have proposed enhancing and retarding mechanisms [4,10,78]. However, the effect of gypsum on the kinetic shift from silicate- to aluminate-dominant cement hydration is not completely understood. Thus, the effect of gypsum on aluminate and silicate phase reactions was investigated during cement hydration, considering the complex interactions between their reactions.

Fig. 19 shows that the silicate peak decreased from 6.3 to 2.7 mW•g^{-1}, the silicate peak time increased from 7.0 to 12.1 h, the aluminate peak decreased from 5.8 to 2.4 mW•g^{-1}, and the aluminate peak time increased from 10.0 to 18.0 h when the gypsum content increased from 2.8 to 4.8%. It was found that a higher gypsum content leads to a larger time interval between the silicate and aluminate peaks,

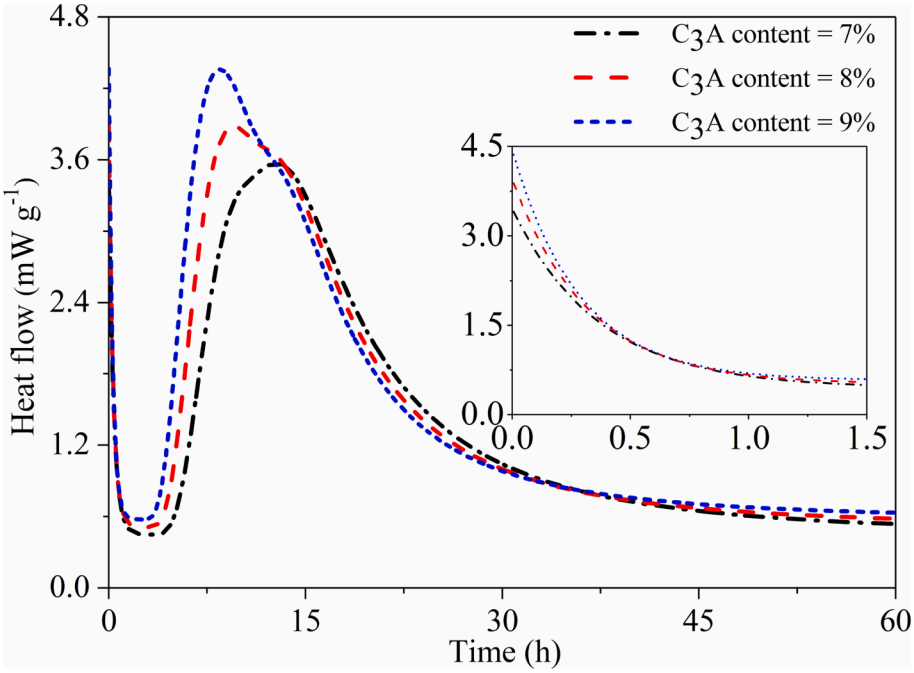

Fig. 20. Effect of C_3A content on hydration heat flow $\dot{Q}$.

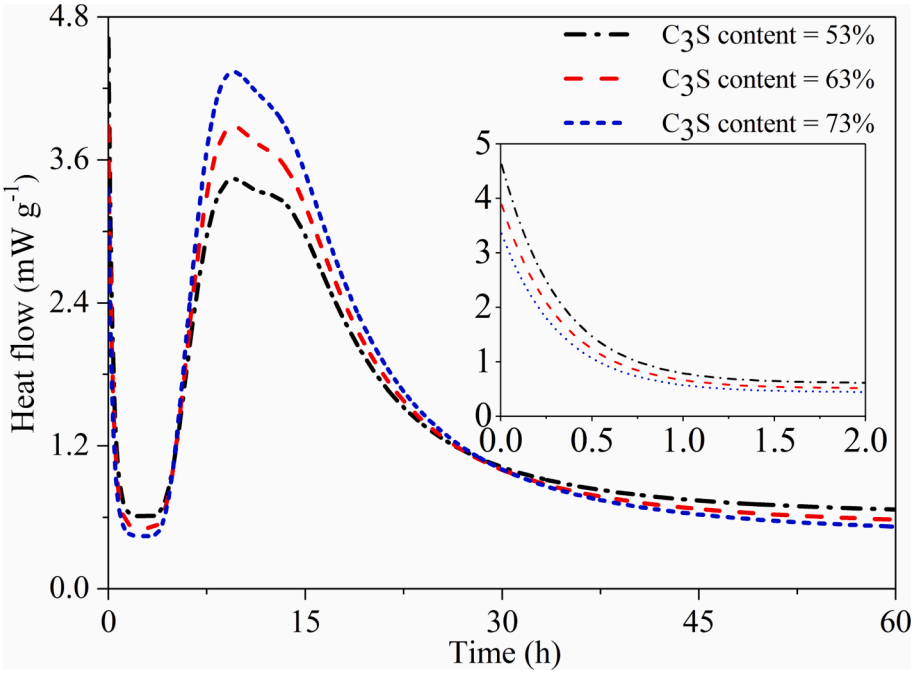

Fig. 21. Effect of C_3S content on hydration heat flow $\dot{Q}$.

as well as more time required to reach the aluminate peak, which indicates that the sulfate ion retards the kinetic shift from silicate- to aluminate-dominant cement hydration. The higher gypsum content released more sulfate ions that were then adsorbed on the C_3S surface and consumed in the ettringite precipitation reaction, prolonging the induction period [8]. Subsequently, a higher gypsum content resulted in the formation of more ettringite, which reduced the surface area available for C-S-H precipitation and thus decreased the silicate peak. A higher gypsum content also exhibited a stronger retarding effect on the aluminate phase reaction [78].

3.3.2. *Effect of C_3A content on kinetics shift*

As reported in the literature, it can be found that the silicate reaction peak is higher than the aluminate reaction peak in several cases, while the aluminate reaction peak is higher than the silicate reaction peak in other cases. This indicates during cement hydration, the reaction kinetics shift from silicate- to aluminate-dominant, indicating that the interactions between silicate and aluminate reactions play a crucial role in the cement hydration reaction mechanism. Although the hydration reaction kinetics of C_3S and C_3A mixtures have also been investigated using the hydration heat flow [10,12,82], the effect of the C_3A content on the kinetic shift is still a topic of debate. Therefore, the effect of C_3A on the kinetic shift was investigated using the heat flow and concentration of the ionic species.

Fig. 20 shows that the silicate peak increased from 3.3 to 4.4 $mW \bullet g^{-1}$, the occurrence time of the silicate peak decreased from 9.9 to 8.4 h, the aluminate peak increased from 3.57 to 3.62 $mW \bullet g^{-1}$, and the occurrence time of the aluminate peak decreased from 12.9 to 12.5 h when the C_3A content increased from 7 to 9%. A higher C_3A content results in a larger difference between the silicate and aluminate peak values and times. The higher C_3A content resulted in more ettringite precipitation during the pre-induction and induction periods, which occupies the grain surface area available for C-S-H precipitation, thereby hindering the C_3S hydration reaction [12]. Meanwhile, more aluminum ions were released during the C_3A dissolution reaction, and the adsorption of aluminum ions on the C_3S surface dissolution sites promoted the inhibition of the C_3S hydration reaction [11,79].

3.3.3. *Effect of C_3S contenton kinetics shift*

Apart from C_3A, the silicate phase mineral is another important aspect of the kinetic shift from silicate- to aluminate-dominant cement hydration. Therefore, the effect of C_3S on the kinetic shift was studied using the silicate and aluminate peaks at different C_3S contents. As shown in Fig. 21, the silicate peak increased from 3.4 to 4.3 $mW \bullet g^{-1}$, the occurrence time of the silicate peak increased from 9.1 to 9.4 h, the aluminate peak increased from 3.2 to 3.8 $mW \bullet g^{-1}$, and the occurrence time of the aluminate peak decreased from 13.9 to 13.5 h when the C_3S content increased from 53 to 73%. It was observed that a higher C_3S content resulted in a larger difference between the silicate and aluminate peak values and a smaller time interval between them. It can be concluded that a higher C_3A/C_3S ratio resulted in a longer time interval between the silicate and aluminate peaks. This may be attributed to the increased C-S-H precipitation originating from the higher C_3S content. Moreover, the absorption of more sulfate ions on the C-S-H surface facilitated the C_3S hydration reaction [8]. Subsequently, sulfate desorption from C-S-H enhances ettringite precipitation owing to C_3A dissolution, leading to a higher aluminate peak [83].

4. Conclusions

To gain deeper insights into the combined effect of multi-mineral dissolution, diffusion, precipitation, adsorption, and interactions on the hydration kinetics shifting from silicate-to aluminate-dominant Portland cement with different mineral compositions, a multi-mineral reactive transport model was proposed without any fitting and changing the parameters for each case. In the model, the reaction rates of each mineral phase dissolution, hydration product precipitation, ion diffusion, ion adsorption, and interaction were calculated and coupled via ionic concentration using the modified PNP equation. The calculated ionic concentration was then used to estimate the hydration heat flow, which was theoretically calculated by the superposition of the reaction rates of the silicate and aluminate phases. The consistency between the simulation and experimental results confirms the predictive accuracy of the proposed model. The effects of dissolution, diffusion, precipitation, and adsorption reactions on the heat flow were studied individually and combined under various conditions. A quantitative analysis of the

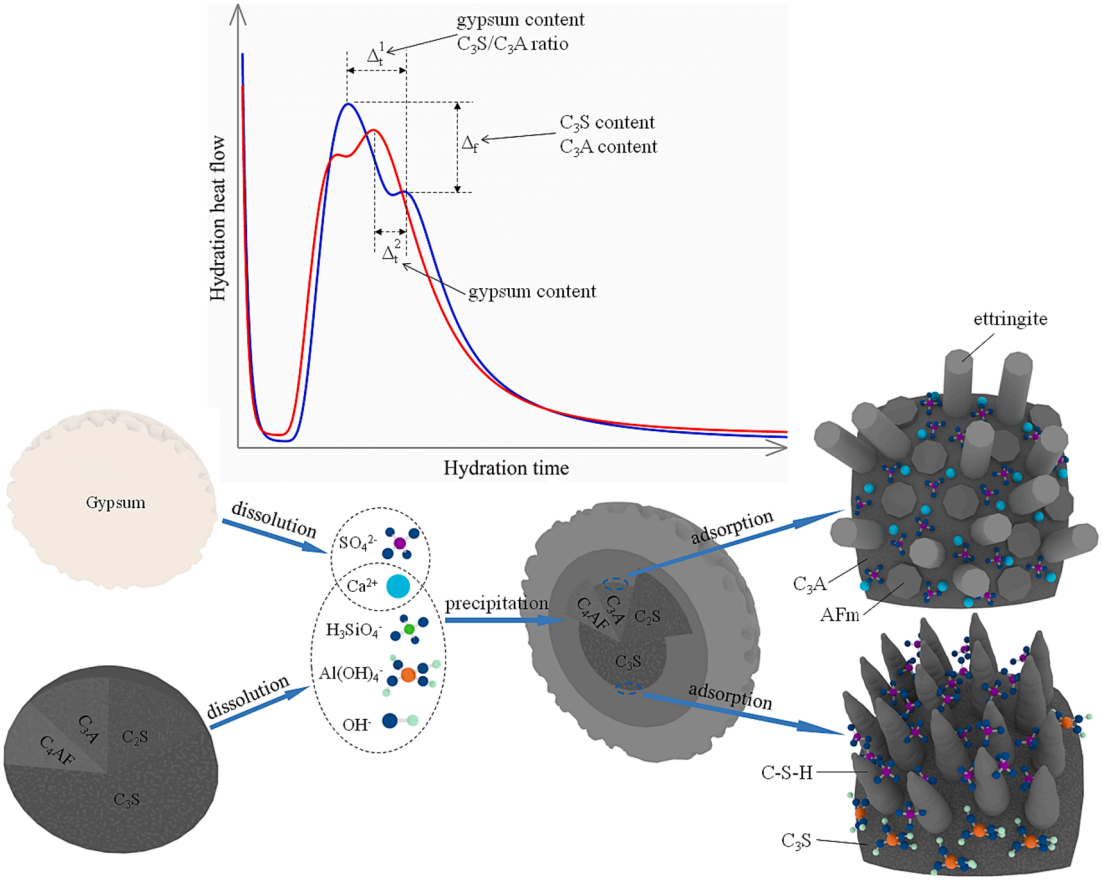

Fig. 22. Effect of multi-mineral reactions and compositions on cement hydration kinetics.

silicate and aluminate peaks was conducted to investigate the combined effect of different mineral compositions on the kinetic shift. Fig. 22 summarizes the main conclusions of this study.

- The faster dissolution of gypsum leads to a larger time interval between the silicate and aluminate peaks, which indicates that the sulfate ion hinders the shifting from silicate, dominating the Portland cement hydration kinetics.
- The faster precipitation of C-S-H results in a larger difference between the silicate and aluminate peak values and times because the sulfate ions absorbed on the C-S-H surface hinder the kinetic shift from silicate to aluminate.
- The diffusion of sulfate ions was significantly affected by gypsum dissolution. The higher solubility constant of gypsum leads to a higher concentration gradient and supersaturation concentration of sulfate ions between the cement and gypsum grains during the initial dissolution of the cement clinker.
- Adsorption of the calcium-sulfate ion pair complex reduced the number of active sites on the C_3A surface, which inhibited C_3A dissolution during the pre-induction and induction periods. The adsorption of sulfate ions on the C-S-H surface promoted the precipitation of C-S-H, which accelerated the C_3S reaction during the acceleration period.
- A higher gypsum content led to a larger time interval between the silicate and aluminate peaks, and more time was required to reach the aluminate peak. A higher C_3S or C_3A content results in a larger difference between the silicate and aluminate peak values. A higher C_3A/C_3S ratio resulted in a longer time interval between the silicate and aluminate peaks.

Furthermore, the model can be extended to study the effect of supplementary cementitious materials, such as fly ash, silica fume, slag, and pozzolanic materials, on cement hydration reaction kinetics. In addition, the model can be modified to reveal the effects of the mineral composition and interactions on the mechanical properties and durability of cementitious materials.

Declaration of Competing Interest

The authors declare that they have no known competing financial interests or personal relationships that could have appeared to influence the work reported in this paper.

Data availability

Data will be made available on request.

Acknowledgments

This work was supported by the Key Research and Development Program of Hubei Province (Grant No. 2020BCB065). The authors would like to express their gratitude to Prof. Jiafu Wang, Jiaheng Lei, and Shumin Zhou for their insightful discussions.

Appendix A. Supplementary data

Supplementary data to this article can be found online at https://doi.org/10.1016/j.matdes.2023.112228.

References

[1] A. Bourchy, L. Barnes-Davin, L. Bessette, J.M. Torrenti, Effect of Cement Composition on Fresh State and Heat of Hydration of Portland Cement with Limestone and Slag, ACI Mater. J. 117 (1) (2020) 153–165.
[2] K. Scrivener, A. Ouzia, P. Juilland, A. Kunhi Mohamed, Advances in understanding cement hydration mechanisms, Cem. Concr. Res. 124 (2019), 105823.
[3] Y. Yan, R. Wang, J. Liu, J. Tang, K.L. Scrivener, Effect of a liquid-type temperature rise inhibitor on cement hydration, Cem. Concr. Res. 140 (2021), 106286.
[4] J.S. Andrade Neto, E.D. Rodríguez, P.J.M. Monteiro, A.G. De la Torre, A. P. Kirchheim, Hydration of C_3S and Al-doped C_3S in the presence of gypsum, Cem. Concr. Res. 152 (2022), 106686.
[5] S. Joseph, J. Skibsted, Ö. Cizer, A quantitative study of the C_3A hydration, Cem. Concr. Res. 115 (2019) 145–159.
[6] Y. Tao, D. Wan, W. Zhang, F. Wang, S. Hu, Intrinsic reactivity and dissolution characteristics of tetracalcium aluminoferrite, Cem. Concr. Res. 146 (2021), 106485.
[7] A.S. Brand, J.M. Gorham, J.W. Bullard, Dissolution rate spectra of β-dicalcium silicate in water of varying activity, Cem. Concr. Res. 118 (2019) 69–83.
[8] J.d.S. Andrade Neto, A.G. De la Torre, A.P. Kirchheim, Effects of sulfates on the hydration of Portland cement – A review, Constr. Build. Mater. 279 (2021), 122428.
[9] Y. Liu, M. Liu, G. Luo, H. Li, H. Tan, Q. Liu, A multiphysics-multiscale-multidrive theoretical model for C3S hydration, Ceram. Int. 49 (1) (2023) 974–985.
[10] F. Zunino, K. Scrivener, Factors influencing the sulfate balance in pure phase C_3S/C_3A systems, Cem. Concr. Res. 133 (2020), 106085.
[11] E. Pustovgar, R.K. Mishra, M. Palacios, J.-B. d'Espinose de Lacaillerie, T. Matschei, A.S. Andreev, H. Heinz, R. Verel, R.J. Flatt, Influence of aluminates on the hydration kinetics of tricalcium silicate, Cem. Concr. Res. 100 (2017) 245–262.
[12] S.T. Bergold, F. Goetz-Neunhoeffer, J. Neubauer, Interaction of silicate and aluminate reaction in a synthetic cement system: Implications for the process of alite hydration, Cem. Concr. Res. 93 (2017) 32–44.
[13] Y. Liu, H. Li, M. Liu, G. Luo, H. Tan, Q. Liu, Role of ionic diffusion in heat flow and chemical shrinkage of tricalcium aluminate hydration subjected to thermo-chemo-electrical coupled fields, J. Mater. Res. Technol. 23 (2023) 5341–5356.
[14] D.P. Bentz, Three-Dimensional Computer Simulation of Portland Cement Hydration and Microstructure Development, J. Am. Ceram. Soc. 80 (1) (1997) 3–21.
[15] G. Ye, K. van Breugel, A.L.A. Fraaij, Three-dimensional microstructure analysis of numerically simulated cementitious materials, Cem. Concr. Res. 33 (2) (2003) 215–222.
[16] S. Bishnoi, K.L. Scrivener, μic: A new platform for modelling the hydration of cements, Cem. Concr. Res. 39 (4) (2009) 266–274.
[17] J.W. Bullard, E. Enjolras, W.L. George, S.G. Satterfield, J.E. Terrill, A parallel reaction-transport model applied to cement hydration and microstructure development, Model. Simul. Mater. Sci. Eng. 18 (2) (2010), 025007.
[18] N.L.B. Le, M. Stroeven, L.J. Sluys, P. Stroeven, A novel numerical multi-component model for simulating hydration of cement, Comput. Mater. Sci 78 (2013) 12–21.
[19] B. Ma, G. Dui, Z. Jia, B. Yang, C. Yang, Q. Gao, L. Qin, J. Ma, A Simple Cement Hydration Model Considering the Influences of Water-to-Cement Ratio and Mineral Composition, Comp. Model. Eng. Sci. 127 (3) (2021) 1059–1067.
[20] N. Holmes, M. Tyrer, R. West, A. Lowe, D. Kelliher, Using PHREEQC to model cement hydration, Constr. Build. Mater. 319 (2022), 126129.
[21] K.-B. Park, N.-Y. Jee, I.-S. Yoon, H.-S. Lee, Prediction of Temperature Distribution in High-Strength Concrete Using Hydration Model, ACI Mater. J. 105 (2) (2008) 180–186.
[22] N. Meller, C. Hall, A.C. Jupe, S.L. Colston, S.D.M. Jacques, P. Barnes, J. Phipps, The paste hydration of brownmillerite with and without gypsum: a time resolved synchrotron diffraction study at 30, 70, 100 and 150 °C, J. Mater. Chem. 14 (3) (2004) 428–435.
[23] L. Nicoleau, A. Nonat, D. Perrey, The di- and tricalcium silicate dissolutions, Cem. Concr. Res. 47 (2013) 14–30.
[24] J.W. Bullard, J. Hagedorn, M.T. Ley, Q.N. Hu, W. Griffin, J.E. Terrill, A critical comparison of 3D experiments and simulations of tricalcium silicate hydration, J. Am. Ceram. Soc. 101 (4) (2018) 1453–1470.
[25] C. Naber, F. Bellmann, J. Neubauer, Influence of w/s ratio on alite dissolution and C-S-H precipitation rates during hydration, Cem. Concr. Res. 134 (2020), 106087.
[26] N. Maach, J.F. Georgin, S. Berger, J. Pommay, Chemical mechanisms and kinetic modeling of calcium aluminate cements hydration in diluted systems: Role of aluminium hydroxide formation, Cem. Concr. Res. 143 (2021), 106380.
[27] A. Michel, V. Marcos-Meson, W. Kunther, M.R. Geiker, Microstructural changes and mass transport in cement-based materials: A modeling approach, Cem. Concr. Res. 139 (2021), 106285.
[28] E. Samson, G. Lemaire, J. Marchand, J.J. Beaudoin, Modeling chemical activity effects in strong ionic solutions, Comput. Mater. Sci 15 (3) (1999) 285–294.
[29] D. Wagner, F. Bellmann, J. Neubauer, Influence of aluminium on the hydration of triclinic C_3S with addition of KOH solution, Cem. Concr. Res. 137 (2020), 106198.
[30] L. Li, C.I. Steefel, L. Yang, Scale dependence of mineral dissolution rates within single pores and fractures, Geochim. Cosmochim. Acta 72 (2) (2008) 360–377.
[31] K. Maher, C.I. Steefel, D.J. DePaolo, B.E. Viani, The mineral dissolution rate conundrum: Insights from reactive transport modeling of U isotopes and pore fluid chemistry in marine sediments, Geochim. Cosmochim. Acta 70 (2) (2006) 337–363.
[32] J.W. Bullard, G.W. Scherer, J.J. Thomas, Time dependent driving forces and the kinetics of tricalcium silicate hydration, Cem. Concr. Res. 74 (2015) 26–34.
[33] M. Gottapu, J.J. Biernacki, J. Bullard, A Multi-Ionic Continuum-Based Model for C_3S Hydration, J. Am. Ceram. Soc. 98 (10) (2015) 3029–3041.
[34] A. Kumar, S. Bishnoi, K.L. Scrivener, Modelling early age hydration kinetics of alite, Cem. Concr. Res. 42 (7) (2012) 903–918.
[35] A. Soive, V.Q. Tran, External sulfate attack of cementitious materials: New insights gained through numerical modeling including dissolution/precipitation kinetics and surface complexation, Cem. Concr. Compos. 83 (2017) 263–272.
[36] G.W. Scherer, J. Zhang, J.J. Thomas, Nucleation and growth models for hydration of cement, Cem. Concr. Res. 42 (7) (2012) 982–993.
[37] A. Kumar, J. Reed, G. Sant, Vertical Scanning Interferometry: A New Method to Measure the Dissolution Dynamics of Cementitious Minerals, J. Am. Ceram. Soc. 96 (9) (2013) 2766–2778.
[38] P. Feng, S. Ye, N.S. Martys, J.W. Bullard, Hydrodynamic factors influencing mineral dissolution rates, Chem. Geol. 541 (2020), 119578.
[39] L. De Windt, P. Chaurand, J. Rose, Kinetics of steel slag leaching: Batch tests and modeling, Waste Manag. 31 (2) (2011) 225–235.
[40] J. Tang, J.W. Bullard, L.N. Perry, P. Feng, J. Liu, An empirical rate law for gypsum powder dissolution, Chem. Geol. 498 (2018) 96–105.
[41] F. Bellmann, G.W. Scherer, Analysis of C-S-H growth rates in supersaturated conditions, Cem. Concr. Res. 103 (2018) 236–244.
[42] S. Pourchet, L. Regnaud, J.P. Perez, A. Nonat, Early C_3A hydration in the presence of different kinds of calcium sulfate, Cem. Concr. Res. 39 (11) (2009) 989–996.
[43] E. Poupelloz, S. Gauffinet, A. Nonat, Study of nucleation and growth processes of ettringite in diluted conditions, Cem. Concr. Res. 127 (2020), 105915.
[44] C.A.J. Appelo, The anion exchange properties of AFm (hydrocalumite-group) minerals defined from solubility experiments and crystallographic information, Cem. Concr. Res. 140 (2021), 106270.
[45] M. Salgues, A. Sellier, S. Multon, E. Bourdarot, E. Grimal, DEF modelling based on thermodynamic equilibria and ionic transfers for structural analysis, Eur. J. Environ. Civ. Eng. 18 (4) (2014) 377–402.
[46] X. Zhao, Z. Li, W. Tang, X. Gu, Competitive kinetics of Ni(II)/Co(II) and Cr(VI)/P (V) adsorption and desorption on goethite: A unified thermodynamically based model, J. Hazard. Mater. 423 (2022), 127028.
[47] Z. Lu, X. Kong, D. Jansen, C. Zhang, J. Wang, X. Pang, J. Yin, Towards a further understanding of cement hydration in the presence of triethanolamine, Cem. Concr. Res. 132 (2020), 106041.
[48] W. Nocuń-Wczelik, Differential calorimetry as a tool in the studies of cement hydration kinetics with sulphate and nitrate solutions, J. Therm. Anal. Calorim. 130 (1) (2017) 249–259.
[49] E. Hernandez-Bautista, D.P. Bentz, S. Sandoval-Torres, P.F.d.J. Cano-Barrita, Numerical simulation of heat and mass transport during hydration of Portland cement mortar in semi-adiabatic and steam curing conditions, Cem. Concr. Compos. 69 (2016) 38–48.
[50] P. Li, Z. Jiang, X. An, K. Maekawa, S. Du, Time-dependent retardation effect of epoxy latexes on cement hydration: Experiments and multi-component hydration model, Constr. Build. Mater. 320 (2022), 126282.
[51] T. Qi, W. Zhou, X. Liu, Q. Wang, S. Zhang, Predictive Hydration Model of Portland Cement and Its Main Minerals Based on Dissolution Theory and Water Diffusion Theory, Materials 14 (3) (2021) 595–626.
[52] P. Xueyu, M. Christian, Modeling cement hydration by connecting a nucleation and growth mechanism with a diffusion mechanism. Part II: Portland cement paste hydration, Sci. Eng. Compos. Mater. 23 (6) (2016) 605–615.
[53] S.J. Preece, J. Billingham, A.C. King, On the initial stages of cement hydration, J. Eng. Math. 40 (1) (2001) 43–58.
[54] Y. Cao, L. Guo, B. Chen, J. Wu, Effect of pre-introduced sodium chloride on cement hydration process, Adv. Cem. Res. 33 (12) (2021) 526–539.
[55] Z. Lu, X. Kong, C. Zhang, D. Jansen, J. Neubauer, F. Goetz-Neunhoeffer, Effects of two oppositely charged colloidal polymers on cement hydration, Cem. Concr. Compos. 96 (2019) 66–76.
[56] E. Kuzielová, M. Žemlička, R. Novotný, M.T. Palou, Simultaneous effect of silica fume, metakaolin and ground granulated blast-furnace slag on the hydration of multicomponent cementitious binders, J. Therm. Anal. Calorim. 136 (4) (2019) 1527–1537.
[57] A. Schöler, B. Lothenbach, F. Winnefeld, M.B. Haha, M. Zajac, H.-M. Ludwig, Early hydration of SCM-blended Portland cements: A pore solution and isothermal calorimetry study, Cem. Concr. Res. 93 (2017) 71–82.
[58] D. Jansen, J. Neubauer, F. Goetz-Neunhoeffer, R. Haerzschel, W.D. Hergeth, Change in reaction kinetics of a Portland cement caused by a superplasticizer — Calculation of heat flow curves from XRD data, Cem. Concr. Res. 42 (2) (2012) 327–332.
[59] A. Ouzia, K. Scrivener, The needle model: A new model for the main hydration peak of alite, Cem. Concr. Res. 115 (2019) 339–360.
[60] M.G. Chaei, A. Akbarnezhad, A. Castel, R. Lloyd, L. Keyte, S. Foster, Precision of cement hydration heat models in capturing the effects of SCMs and retarders, Mag. Concr. Res. 70 (23) (2018) 1217–1231.
[61] P. Juilland, A. Kumar, E. Gallucci, R.J. Flatt, K.L. Scrivener, Effect of mixing on the early hydration of alite and OPC systems, Cem. Concr. Res. 42 (9) (2012) 1175–1188.
[62] L.G. Briendl, C. Grengg, B. Müller, G. Koraimann, F. Mittermayr, P. Steiner, I. Galan, In situ pH monitoring in accelerated cement pastes, Cem. Concr. Res. 157 (2022), 106808.
[63] A. Younsi, A. Bordy, S. Aggoun, B. Fiorio, Hydration-drying interactions in OPC pastes blended with recycled OPC paste fine powder: Critical curing relative humidity hampering hydration, Constr. Build. Mater. 190 (2018) 403–413.

[64] R.J. Myers, G. Geng, E.D. Rodriguez, P. da Rosa, A.P. Kirchheim, P.J.M. Monteiro, Solution chemistry of cubic and orthorhombic tricalcium aluminate hydration, Cem. Concr. Res. 100 (2017) 176–185.
[65] A.P. Kirchheim, V. Fernàndez-Altable, P.J.M. Monteiro, D.C.C. Dal Molin, I. Casanova, Analysis of cubic and orthorhombic C3A hydration in presence of gypsum and lime, J. Mater. Sci. 44 (8) (2009) 2038–2045.
[66] A.S. Brand, J.W. Bullard, Dissolution Kinetics of Cubic Tricalcium Aluminate Measured by Digital Holographic Microscopy, Langmuir 33 (38) (2017) 9645–9656.
[67] R.K. Mishra, L. Fernández-Carrasco, R.J. Flatt, H. Heinz, A force field for tricalcium aluminate to characterize surface properties, initial hydration, and organically modified interfaces in atomic resolution, Dalton Trans. 43 (27) (2014) 10602–10616.
[68] J. Lapeyre, H. Ma, M. Okoronkwo, G. Sant, A. Kumar, Influence of water activity on hydration of tricalcium aluminate-calcium sulfate systems, J. Am. Ceram. Soc. 103 (6) (2020) 3851–3870.
[69] G. Geng, R.J. Myers, Y.-S. Yu, D.A. Shapiro, R. Winarski, P.E. Levitz, D.A. L. Kilcoyne, P.J.M. Monteiro, Synchrotron X-ray nanotomographic and spectromicroscopic study of the tricalcium aluminate hydration in the presence of gypsum, Cem. Concr. Res. 111 (2018) 130–137.
[70] M.E. Tadros, J.A.N. Skalny, R.S. Kalyoncu, Early Hydration of Tricalcium Silicate, J. Am. Ceram. Soc. 59 (7–8) (1976) 344–347.
[71] A. Sobolkina, V. Mechtcherine, S.T. Bergold, J. Neubauer, C. Bellmann, V. Khavrus, S. Oswald, A. Leonhardt, W. Reschetilowski, G. Scherer, Effect of Carbon-Based Materials on the Early Hydration of Tricalcium Silicate, J. Am. Ceram. Soc. 99 (6) (2016) 2181–2196.
[72] F. Bellmann, H.-M. Ludwig, Analysis of aluminum concentrations in the pore solution during hydration of tricalcium silicate, Cem. Concr. Res. 95 (2017) 84–94.
[73] C. Naber, F. Bellmann, T. Sowoidnich, F. Goetz-Neunhoeffer, J. Neubauer, Alite dissolution and C-S-H precipitation rates during hydration, Cem. Concr. Res. 115 (2019) 283–293.
[74] T. Sowoidnich, F. Bellmann, D. Damidot, H.-M. Ludwig, New insights into tricalcium silicate hydration in paste, J. Am. Ceram. Soc. 102 (5) (2019) 2965–2976.
[75] L. Huang, L. Tang, H. Gu, Z. Li, Z. Yang, New insights into the reaction of tricalcium silicate (C3S) with solutions to the end of the induction period, Cem. Concr. Res. 152 (2022), 106688.
[76] P. Bénard, S. Garrault, A. Nonat, C. Cau-dit-Coumes, Influence of orthophosphate ions on the dissolution of tricalcium silicate, Cem. Concr. Res. 38 (10) (2008) 1137–1141.
[77] H.M. Jennings, The Developing Microstructure in Portland Cement, in: S.N. Ghosh (Ed.), Advances in Cement Technology, Pergamon1983, pp. 349-396.
[78] X. Liu, P. Feng, C. Lyu, S. Ye, The role of sulfate ions in tricalcium aluminate hydration: New insights, Cem. Concr. Res. 130 (2020), 105973.
[79] K. Zhang, P. Shen, L. Yang, M. Rao, F. Wang, Improvement of the Hydration Kinetics of High Ferrite Cement: Synergic Effect of Gypsum and C_3S–C_4AF Systems, ACS Sustain. Chem. Eng. 9 (45) (2021) 15127–15137.
[80] V.K. Peterson, D.A. Neumann, R.A. Livingston, Hydration of Tricalcium and Dicalcium Silicate Mixtures Studied Using Quasielastic Neutron Scattering, J. Phys. Chem. B 109 (30) (2005) 14449–14453.
[81] Z. Zhu, W. Xu, H. Chen, Y. Wang, X. Gou, L. Liu, Y. Gu, Diffusivity of cement paste via a continuum-based microstructure and hydration model: Influence of cement grain shape, Cem. Concr. Compos. 118 (2021), 103920.
[82] A. Quennoz, K.L. Scrivener, Interactions between alite and C_3A-gypsum hydrations in model cements, Cem. Concr. Res. 44 (2013) 46–54.
[83] F. Zunino, K. Scrivener, The influence of the filler effect on the sulfate requirement of blended cements, Cem. Concr. Res. 126 (2019), 105918.